



RESEARCH ARTICLE

10.1029/2023JD039045

The Precipitation Characteristics of Mesoscale Convective Systems Over Europe

Nicolas A. Da Silva¹  and Jan O. Haerter^{1,2,3}

¹Leibniz Centre for Tropical Marine Research, Complexity and Climate, Bremen, Germany, ²Physics and Earth Sciences, Constructor University Bremen, Bremen, Germany, ³Niels Bohr Institute, University of Copenhagen, Copenhagen, Denmark

Key Points:

- Mesoscale convective systems (MCSs) substantially contribute to precipitation and dominate event-based precipitation extremes over Europe
- MCS's diurnal cycle displays a large variability over the coasts and exhibits nocturnal peaks over some continental areas
- The annual cycle of MCS precipitation is attributed to the annual cycle of surface temperature, convective instability, and frontal activity

Supporting Information:

Supporting Information may be found in the online version of this article.

Correspondence to:

N. A. Da Silva,
nicolas.da-silva@leibniz-zmt.de

Citation:

Da Silva, N. A., & Haerter, J. O. (2023). The precipitation characteristics of mesoscale convective systems over Europe. *Journal of Geophysical Research: Atmospheres*, 128, e2023JD039045. <https://doi.org/10.1029/2023JD039045>

Received 10 APR 2023

Accepted 13 NOV 2023

Author Contributions:

Conceptualization: Nicolas A. Da Silva
Data curation: Nicolas A. Da Silva
Formal analysis: Nicolas A. Da Silva, Jan O. Haerter
Funding acquisition: Jan O. Haerter
Investigation: Nicolas A. Da Silva, Jan O. Haerter
Methodology: Nicolas A. Da Silva, Jan O. Haerter
Supervision: Jan O. Haerter
Writing – original draft: Nicolas A. Da Silva

© 2023. The Authors.

This is an open access article under the terms of the [Creative Commons Attribution License](https://creativecommons.org/licenses/by/4.0/), which permits use, distribution and reproduction in any medium, provided the original work is properly cited.

Abstract Mesoscale convective systems (MCSs) are common over Europe and can produce severe weather, including extreme precipitation that leads to flash floods. The few studies analyzing the climatological characteristics of MCSs over Europe are either focusing on only few years of data or on limited subareas. Using the recent Integrated MultisatellitE Retrievals for Global Precipitation Measurement (IMERG) satellite precipitation climatology, we identify and track MCSs for 16 years over Europe. The tracking algorithm relies on the overlap of precipitation features between consecutive time steps and, unlike previous studies, uses lightning data to distinguish convective from stratiform rain patches, which can reduce potential identification errors. We analyze this new European MCS climatology to characterize MCS precipitation properties and conclude the following results: MCSs overall occur most frequently over the Mediterranean and Atlantic during fall and winter, whereas during summer, they concentrate over the continent. Typically, more than a third of seasonal precipitation can be attributed to MCSs, and their contribution to extreme precipitation is even greater, often exceeding 60%. MCSs over the continent display a clear diurnal cycle peak during the afternoon, and some continental areas also show a second, nocturnal peak. The MCS diurnal cycle for coastal and oceanic regions is more variable. We find that the spatiotemporal distribution of MCS precipitation can be attributed to specific environmental variables, namely (sea) surface temperature, fronts occurrence and convective instability. While inland MCS precipitation is mostly constrained by thermodynamics, for the coastal MCSs the atmospheric dynamics plays an important role as well.

Plain Language Summary Extreme precipitation events leading to flash floods have major socioeconomical impacts over Europe. These events are often created by large and long-lived clusters of clouds called mesoscale convective systems (MCSs). Although these MCSs are well known by the climate community, their precipitation characteristics over Europe are not fully documented. This is the purpose of this study. Here, we identify MCSs by using satellite images (detecting precipitation) and lightning flashes for 16 years over Europe. We also develop a tracking algorithm, enabling us to follow each MCS in time and space. The recognition of individual MCSs is based on the overlap of precipitation patches between two consecutive satellite images. We find that MCSs overall occur most frequently over the Mediterranean and Atlantic during fall and winter, whereas during summer, they concentrate over the continent. We show that they substantially contribute to the yearly total precipitation over Europe. More remarkably, MCS is the most frequent cloud organization form responsible for extreme precipitation events over Europe. Thus, the present study gives some general explanations on their main behavior. Also, it is of critical importance to further understand European MCSs and their potential changes in a warming climate.

1. Introduction

Mesoscale convective systems (MCSs) are aggregates of cumulonimbus clouds spanning a few hundreds of kilometers horizontally (Houze, 2018). These organized weather systems are abundant over the tropics where they contribute to more than half of the total precipitation (Feng et al., 2021; Laing & Fritsch, 1997; Liu & Zipser, 2015; Nesbitt et al., 2006; Schumacher & Rasmussen, 2020; Tan et al., 2015). Despite the frequent occurrence of stratiform precipitation from extratropical cyclones in midlatitudes, MCSs are also a significant contributor to midlatitude precipitation (Feng et al., 2021; Haberlie & Ashley, 2019), in particular during summer when thunderstorm activity is most pronounced (Taszarek et al., 2019). In addition to their significant impact on the hydrological cycle, MCSs are often associated with severe weather such as heavy rainfall, large hail, strong winds, or tornadoes (Ashley et al., 2019; Fowler et al., 2021; Jirak et al., 2003; Luo et al., 2020; Mathias et al., 2017; Schumacher & Rasmussen, 2020). In fact, MCS areas and rain intensities tend to be larger in midlatitudes than

Writing – review & editing: Nicolas A. Da Silva, Jan O. Haerter

in the tropics, possibly due to larger wind shear (Schumacher & Rasmussen, 2020). It is therefore important to understand the characteristics of midlatitude MCSs and how these may change with global change.

Several studies have focused on the climatological properties of MCSs around the globe. Over the contiguous United States (CONUS), MCSs preferentially occur in the Midwest during the warm season and in the midsouth during the cold season (Cui et al., 2020; Haberlie & Ashley, 2019). In the warm season, they were found to emerge along the eastern flank of the Rocky Mountains (Cheeks et al., 2020) in the late afternoon and subsequently propagate eastward, peaking at night in the central great plains (Geerts et al., 2017). It was suggested that the nocturnal MCS precipitation peak might be related to the peak in the Low Level Jet (LLJ, Pitchford and London (1962)) as well as gravity waves (Parker, 2008) or potential vorticity anomalies (Jirak & Cotton, 2007) generated and advected away from the Rockies. A nocturnal peak in MCS precipitation was also observed in eastern China (Li et al., 2020) and Argentina (Salio et al., 2007). Both regions have a mountain range in their western parts (Tibetan Plateau and Andes, respectively) and thus feature similar topographic characteristics as the midwest CONUS. Conversely, the varied European topography with several mountain ranges oriented along different directions might make for a more complex picture of the MCS diurnal cycle.

Several previous studies that examined MCSs over Europe focus on a restricted part of Europe (García-Herrera et al., 2005; Punkka & Bister, 2015; Rigo et al., 2019; Surowiecki & Taszarek, 2020), investigate only one season (Kolios & Feidas, 2010; Morel & Senesi, 2002), or use a limited time record to assess climatological properties (García-Herrera et al., 2005; Kolios & Feidas, 2010; Morel & Senesi, 2002). Using 5 years of infrared (IR) satellite data, Morel and Senesi (2002) found that summer MCSs (April–September) are more common over land than sea and are triggered near mountainous areas (Pyrenees, Alps, Carpathians) during the afternoon, a general characteristic also found for the CONUS.

This study composes a comprehensive MCS precipitation climatology over Europe from 16 years of the Integrated Multisatellite Retrievals for GPM (IMERG) combined with the European Cooperation for Lightning Detection (EUCLID) data. MCSs were often identified as large contiguous areas of low IR radiation emitted from cold convective anvils. While this approach is successful over the tropics, it may not be appropriate over midlatitudes which are also subject to large frontal non-MCS rainbands that come with similarly low brightness temperatures. Besides, mature convective clouds may also exhibit warmer brightness temperatures while producing lightning (Cecil et al., 2005). This is why more robust methods were recently developed for identifying MCSs in the midlatitudes (Feng et al., 2021), making use of the precipitation field to distinguish between convective and nonconvective systems, since convective cells generally produce more extreme precipitation rates than stratiform-type systems. These methods involve the use of thresholds on the precipitation field and thus rely on its accuracy. Besides, as inconsistencies may exist among these different data sets, an algorithm defining an MCS through the brightness temperature field may miss part of the MCS precipitation. For all these reasons, and since our objective is to determine the contribution of MCSs to precipitation totals, we adopt yet another approach, which instead resorts to lightning flashes. Indeed, lightning is a trademark of convection and can be accurately determined through networks of ground-based lightning detection sensors such as EUCLID (Schulz et al., 2016). The use of a single data set (IMERG) for the tracking ensures self-consistency of our tracked precipitation features.

This study thus aims at characterizing and understanding the hydrological “footprint” and the diurnal cycle of MCS precipitation over Europe. In Section 2, we describe the data sets exploited and how they are used to detect and track MCSs. The contribution of MCSs to both mean and extreme precipitation over Europe, as well as the MCS diurnal cycle, are characterized in Section 3. We then investigate the causes explaining the regional and seasonal differences of MCS precipitation (Section 4). Finally, we discuss our results and conclude the study (Section 5).

2. Data and Tracking Algorithm

Our method shares some aspects with Feng et al. (2021) but primarily defines patches with the precipitation field instead of cloud top brightness temperatures and uses lightning data to distinguish convective patches.

2.1. Observational Data Sets

For each data set, data were extracted for a domain covering most of Europe (−13°W to 38°E, 30°N to 59°N; Figure 1).

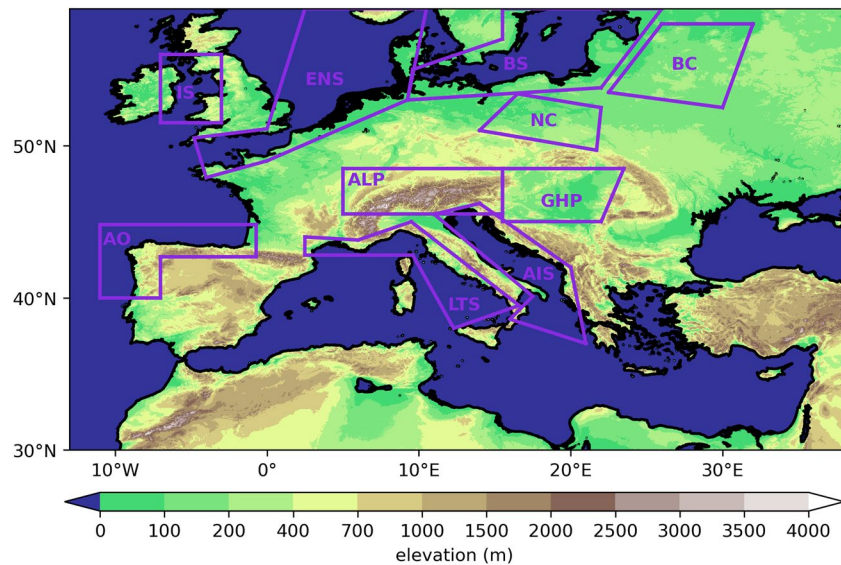


Figure 1. Study domain highlighting subregions: AO for Atlantic Ocean, IS for Irish Sea, ENS for English channel and North Sea, LTS for Ligurian and Tyrrhenian Seas, ALP for Alps, BS for Baltic Sea, AIS for Adriatic and Ionian Seas, NC for north Carpathian, GHP for Great Hungarian Plain and BC for Baltic Continent. The shadings represent the elevation (in m).

2.1.1. Integrated Multisatellite Retrievals (IMERG)

We identify precipitating features (PFs) using the IMERG precipitation product, version V06 B, from the Global Precipitation Measurement (GPM) project (Huffman et al., 2019). This product merges measurements from a constellation of satellites, carrying passive microwave (PM), and/or infrared (IR) sensors. While the PM sensors are generally more precise since they are directly measuring the signal alteration by precipitation droplets, their spatiotemporal coverage is limited. In contrast, IR sensors measure precipitation indirectly through cloud top brightness temperatures, but have a higher spatiotemporal resolution. The precipitation estimates from every satellite are intercalibrated and combined to produce a half-hourly estimate of precipitation at 0.1° of horizontal resolution which is monthly calibrated by the Global Precipitation Climatology Project (GPCP) satellite-gauge product (Adler et al., 2018).

Despite IMERG is known to provide a “robust representation of spatiotemporal patterns of precipitation” (Pradhan et al., 2022), it is worth mentioning that uncertainties in its precipitation estimates exist. Notably, IMERG may be inconsistent between consecutive time steps (as mentioned in Feng et al. (2021)), which may affect the tracking accuracy of the smallest PFs but have limited impacts on MCS PFs. Besides, IMERG may smooth precipitation extremes through its morphing scheme, underestimate warm cloud precipitation (Sungmin & Kirstetter, 2018) and produce errors through imprecise IR estimates (Tan et al., 2016) and limitations in the retrieval algorithm (Oliveira et al., 2016). However, these uncertainties were found to mainly affect the daily and subdaily timescales, and we expect them to have only small impacts on the climatological scale (Pradhan et al., 2022) used in this study. The IMERG product was used in several recent cloud tracking algorithms for studying the properties of convective storms such as MCSs (Feng et al., 2021; Hayden et al., 2021; Takahashi et al., 2021).

2.1.2. European Cooperation for Lightning Detection (EUCLID)

To differentiate convective from stratiform weather systems, we employ the EUCLID lightning data set (Poelman et al., 2016; Schulz et al., 2016). Only cloud to ground lightning flashes (CGs) are used for their homogeneous and continuous high detection efficiency (exceeding 90%) over Europe between 2005 and 2020 (Schulz et al., 2016). The EUCLID lightning location errors generally do not exceed 500 m over Europe, thus reasonably low in comparison to the 0.1° (around 8 km) IMERG grid. The original data set provides the number of CG in 30-min time windows and on a $0.045^\circ \times 0.064^\circ$ grid covering most of Europe. We linearly interpolated the original lightning data set to the IMERG grid ($0.1^\circ \times 0.1^\circ$) to achieve spatial coherence between both data sets. As convection is not necessarily associated with CG, our approach focusing on CGs may underestimate the number of convective systems. For instance, MacGorman et al. (2011) noted that 10–20% of the studied thunderstorms

in the Great Plains produced only intracloud flashes. Nonetheless, it is expected that this underestimation mainly concerns the weakest convective systems with low flash rates (MacGorman et al., 2011).

2.1.3. ECMWF Atmospheric Reanalysis Version 5 (ERA5)

Several variables (SST; 2-m and 600 hPa temperatures; 600 hPa zonal and meridional wind speed; Convective Available Potential Energy (CAPE)) from the ERA5 global reanalysis product (Hersbach et al., 2020) are used to provide insights on the processes involved explaining the spatiotemporal distribution of MCSs over Europe (Section 4). ERA5 is provided as hourly outputs on a 0.25° grid. In this study, the variables mentioned above were selected for the period 2000–2020 and monthly and spatially averaged to determine their annual cycle over specific regions of Europe (Section 4). As ERA5 assimilates the ECMWF Integrated Forecast System (IFS) model forecasts with parameterized convection, the ERA5 representation of convective processes and their effect on environmental variables should be treated with caution. Besides, it was shown that the performances of ERA5 remains low along sharp topographic boundaries such as coasts and mountains (Taszarek et al., 2021). Nevertheless, ERA5 is considered as “one of the most reliable available reanalyses for exploration of convective environments” and it was recently found that convective environment parameters and their annual cycle are well represented within ERA5 over Europe (Taszarek et al., 2021; Varga & Breuer, 2022).

2.1.4. General Bathymetric Chart of the Oceans (GEBCO)

Since mountain ranges were found to play an important role in the genesis of MCSs in midlatitudes (Cheeks et al., 2020; Morel & Senesi, 2002), we also make use of the GEBCO topography data set.

2.2. MCS Tracking Algorithm

2.2.1. Detecting Precipitation Features and Tracks

Similar to Feng et al. (2021), we first apply a spatial filter of 0.3° to IMERG precipitation (Figures 2a and 2b) and define PFs as contiguous patterns (when considering the four nearest neighbors on the regular longitude-latitude IMERG grid) of filtered precipitation above 2 mm hr^{-1} (red contours in Figure 2b). All PFs are labeled at each time step as follows: when a PF spatially overlaps with another PF at the previous time step, it receives the same identification number (IN). To limit identification errors related to fast moving PFs, we adopt the iterative strategy of Moseley et al. (2013) computing the mean displacement of all neighboring PFs within a 1,000 km radius around a nonoverlapping PF, then translating the nonoverlapping PF backward in time with the resulted displacement vector, and searching for overlap in the corresponding new position. We address splitting and merging cases by using the method of Moseley et al. (2019) with a parameter $\theta = 1$ (Figure S1 in Supporting Information S1). An example of a MCS track is provided in Figure 2d where the contours of the MCS at current and previous time steps are highlighted for a better identification of the overlapping areas used for the tracking. In order to define shape properties, such as diameter, orientation, and eccentricity, we then fit an ellipse to each PF and at each time step. The fitting algorithm minimizes the sum of the distances between the contours of the PF and the ellipse in a least square sense (see Figure 2c). The probability density function (PDF) of the ellipse goodness of fit (Figure S2 in Supporting Information S1) and more details about the algorithm are provided as Text S1 in Supporting Information S1.

2.2.2. Defining Convective Precipitation Features and MCSs

We now define convective and stratiform PFs by using the EUCLID lightning data set regridded to match the IMERG grid. At any time of its “life cycle,” a PF which does not fulfill the MCS criteria (defined below) and with at least one CG detected inside its area during the corresponding IMERG 30-min time window is defined as an “isolated convective PF.” In practice, the neighboring IMERG pixels of PFs were also considered for the gathering of CG to account for any spatiotemporal mismatch between IMERG and EUCLID. In this study, a MCS PF is defined with the two following criteria: (a) it has a diameter of at least 100 km for at least four consecutive hours and (b) at least one CG is detected inside or in neighboring IMERG pixels of its area during these four consecutive hours. The remaining of the PFs is defined as stratiform PFs.

Another approach, which makes use of ERA5 CAPE instead of lightning data (described in Text S2 of Supporting Information S1), was tested to define convective PFs and produced similar MCS results to those using CGs (Figures S3 and S4 in Supporting Information S1), showing that the MCS identification is robust. Here we choose to keep using the EUCLID lightning data set for its high accuracy and its finer spatiotemporal resolution

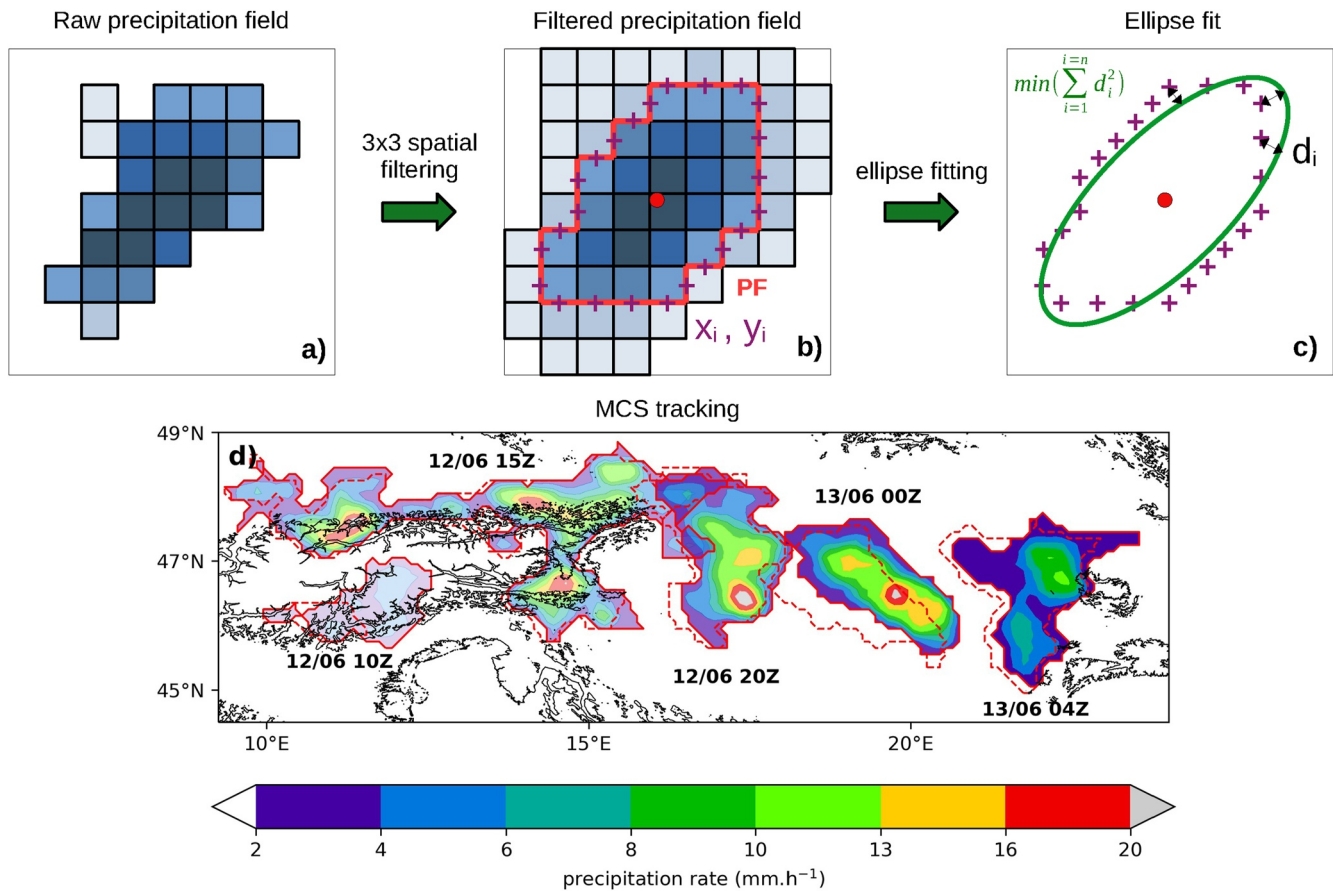


Figure 2. Scheme describing the precipitating feature (PF) identification (a, b) and the ellipse fitting algorithm (c) in this study. First, the Multisatellite Retrievals for Global Precipitation Measurement (IMERG) precipitation field (represented by blue pixels, with darker blue colors standing for more intense precipitation) is spatially filtered (a, b). Second, contours of filtered precipitation above 2 mm h^{-1} are drawn (in red) to define PFs (b). The centers of the edges of the pixel contours (purple crosses) are used to fit an ellipse (in green) to each PF by minimizing the distance between the PF contours and the ellipse (c). Time evolution of a tracked mesoscale convective system (MCS) over the Alps and the Great Hungarian Plain during 10:00 UTC 12 June 2018 to 04:00 UTC 13 June 2018 (d). The snapshots show 10:00 UTC, 15:00 UTC, 20:00 UTC on 12 June 2018 and 00:00 UTC and 04:00 UTC on 13 June 2018 for the spatially filtered IMERG precipitation field (in mm/h). Plain (dashed) red contours delimit the MCS at (respectively, the previous IMERG time step of) each snapshot.

(Section 2.1). Figure 3a is a snapshot of IMERG precipitation, EUCLID CGs, and the objects detected by our algorithm on 9 June 2014 at 21h45 UTC, where intense MCSs associated with severe weather were observed in western Europe (Mathias et al., 2017). It shows a general good correspondence between the CGs and the precipitating cells emerging from two different data sets, as well as fairly consistent ellipse fits to these objects. One can see that with the threshold approach for the definition of PFs, only the most intense precipitating cells are detected as PF by the algorithm.

For the analysis in the current work, we retain unfiltered precipitation from the original IMERG grid. Since the PFs are defined using the spatial average of IMERG precipitation from 3×3 grid points, all of these unfiltered IMERG precipitation grid points contributing to the spatially filtered precipitation field of a particular PF are retained for this PF. This procedure may result in precipitation grid boxes belonging to two (or more) PFs at the same moment. We have checked the PDFs with and without these repeated pixels and found that the differences are minor (not shown) and therefore retained this approach.

3. MCS Climatology Over Europe

3.1. Overall Characteristics—MCSs Are More Than a Sum of Stratiform and Convective Cells

By using the tracking algorithm described above, we were able to detect a total of 11,746 MCSs from 2005 to 2020 (on average 734 per year) in the European domain (Figure 1). To give an overview, Figure 3b shows the

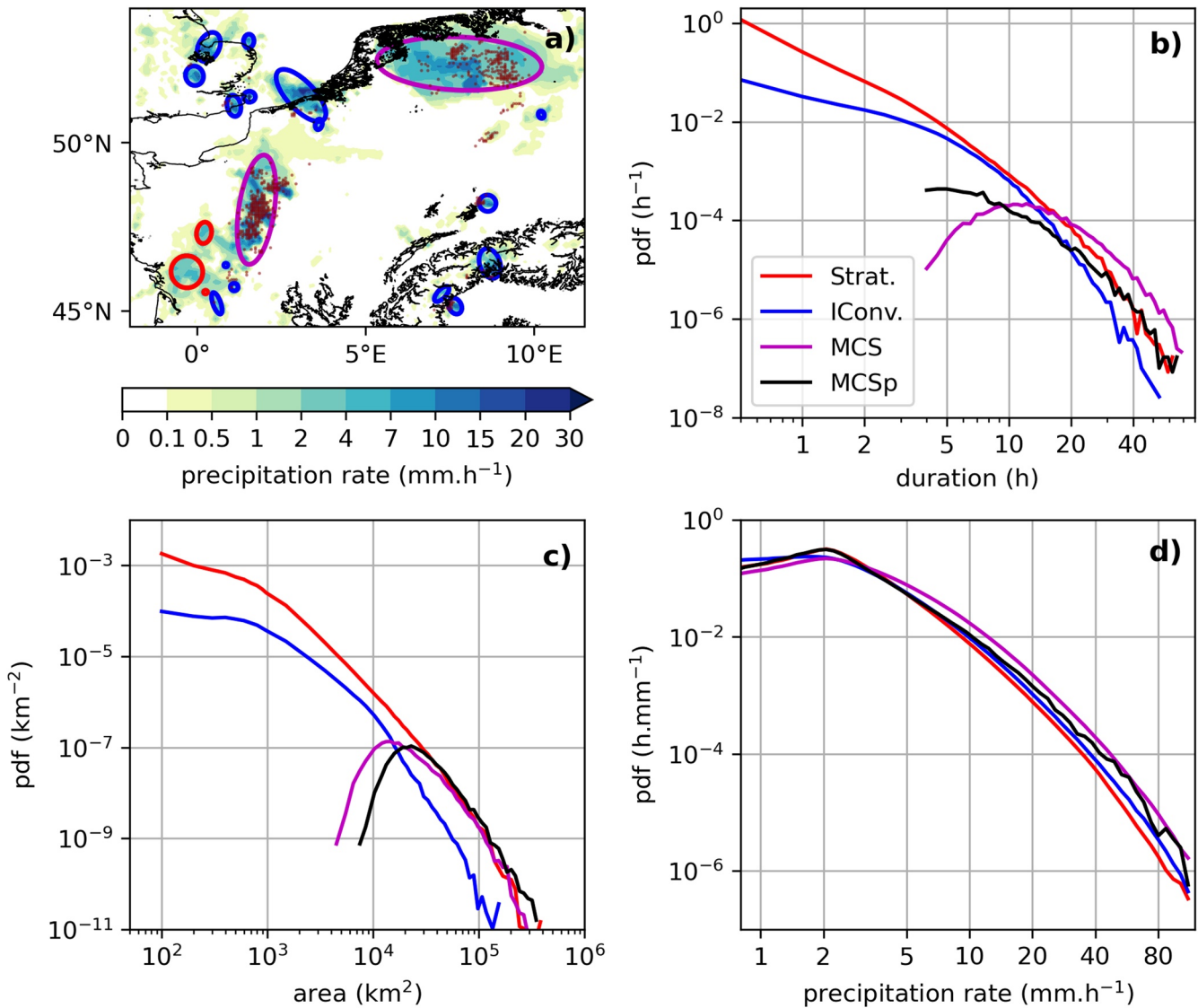


Figure 3. Snapshot of Multisatellite Retrievals for Global Precipitation Measurement (IMERG) precipitation (shadings; in mm hr^{-1}) and European Cooperation for Lightning Detection (EUCLID) CGs (dark red points) on 9 June 2014 at 21h45 UTC in western Europe (a). The ellipses represent the detected precipitating features (PFs) according to our algorithm presented in Section 2: red for stratiform PFs, blue for isolated convective PFs, and magenta for mesoscale convective system (MCS) PFs. Probability density functions (PDF) of PF duration (b; in h), mean area (c; in km^2), and precipitation (d; in mm hr^{-1}) for stratiform (“Strat.,” red), isolated convective (“IConv.,” blue), MCS PFs (magenta), and for MCS periods (“MCSp,” black). MCSp was built by selecting only instants for which a MCS PF has MCS attributes (see section 3a). The probability density function (PDF) of duration and area were normalized by the total number of PFs while the PDF of precipitation were normalized by the number of instants of PFs of the corresponding type (stratiform, isolated convective, MCS, or MCS periods).

PDF of the duration of detected PFs for the different types (stratiform, isolated convective, MCS; defined in Section 2.2). We also include the PDF of MCS periods (MCSp) defined as MCS PFs at instants for which there exists a 4-hr period within the MCS PF lifetime that (a) contains this instant, (b) in which the MCS PF has a diameter that exceeds 100 km, and (c) in which at least one CG was detected inside or in a neighboring IMERG pixel of the MCS PF area (defining the MCS criteria; Section 2.2). Since MCSs are sometimes embedded in fronts, the duration of PFs classified as MCS can reach several days whereas the actual MCS period may only last for few hours. For stratiform and isolated convective precipitation, the PDF monotonically decreases with PF duration. Isolated convective PFs show a reduced spread in the distribution compared to the stratiform cases. This is seen by the stronger curvature of the blue curve compared to the red, in agreement with previously reported data by Berg and Haerter (2013) but for local rain durations in Germany. We find typical MCS lifetimes to be around 10 hr when accounting for inactive periods, whereas durations of active MCS periods are only about half the total

MCS lifetime. The area distribution (Figure 3c) closely mirrors that of duration. MCS areas show an even smaller spread, with occurrence frequencies peaking around 10^4 km², which is partly influenced by our detection method enforcing a diameter threshold of 100 km. The PDF of mean precipitation rate (Figure 3d) shows that the occurrence of high precipitation intensities, that is, exceeding 10 mm hr⁻¹, is approximately three times more frequent within MCSs than for isolated convective PFs, and precipitation intensities of isolated convective PFs are overall more intense than stratiform ones. The maximum around 2 mm hr⁻¹ can be attributed to our detection threshold.

Given the intensity distributions (Figure 3d), MCSs cannot be only seen as a random collection of stratiform and isolated convective precipitation patches but as a collection of these skewed toward high precipitation. The higher proportion of extreme precipitation within MCSs may result from the merging of convective cells, possibly related to dynamical (cold pools and/or mesoscale circulation; e.g., Haerter & Schlemmer, 2018) and/or micro-physical effects (reduced entrainment and/or rain evaporation; e.g., Da Silva et al., 2021).

3.2. MCSs Dominate in Southern Coastal Regions in Winter and Continental Regions in Summer

As noted (Taszarek et al., 2019), midlatitude convection is strongly dependent on season, a feature we investigate further by distinguishing MCS occurrence for the different months (Figure 4). MCSs are generally more frequent in the coastal regions of southern Europe in fall (SON) and winter (DJF), whereas they dominate northern continental regions in summer (JJA), a pattern resembling that of the overall precipitation climatology in Europe (Figure S5 in Supporting Information S1).

During fall, the overall highest MCS frequency (approximately six per month) is reached in November along Eastern Adriatic, while MCSs of the remaining Mediterranean and the continental regions at similar latitude are 2–3 times less frequent. Local maxima in MCS frequency are also seen in northwestern Spain or the Italian west coast, where frequencies are again much greater than for other regions of similar latitude. Although declining, this intense MCS activity persists in winter over the same regions. As opposed to the strong activity during fall, the transitional period during spring (MAM) shows generally weak MCS activity. This lack of symmetry regarding MCSs during the transitional periods points to a strong influence of the large water bodies on MCSs. Indeed, due to their large heat capacity (thus memory), the seas are warmer in fall than in spring whereas continental temperatures are fairly similar between both seasons. Summertime MCSs, for example, from June to August, are most frequent over the Alps, reaching about five per month in August. To a lesser extent, a local maximum in MCS frequency is also present for the Carpathians, highlighting the role of topography in triggering or enhancing deep convection (Houze & Robert, 2012). Perhaps more surprisingly, the continental regions near the East of southern Baltic Sea experience a pronounced peak of MCS occurrence during the month of July, with around 3.5 MCSs in this month on average. Another remarkable feature is the high number (exceeding four on average) of MCSs in both the southern Baltic Sea and the southern North Sea (especially in the southeastern side) during August, while the surrounding continental areas experience comparably fewer MCSs. Finally, one may notice that northern Germany experiences fewer MCSs than its surrounding regions between June and September. This may be due to the Alps acting as a barrier to some of the MCSs, which mostly travel in southwesterly flows (not shown).

Similarities between the spatial distribution of MCS occurrence in our current study and previous studies exist for the summer months. Yet, there are some noticeable differences compared to the previous climatologies of summer MCSs (Kolios & Feidas, 2010; Morel & Senesi, 2002). While some of the difference might be explained by the longer averaging time used by the present study, an important difference lies in our method identifying MCSs by precipitation and lightning, whereas both Morel and Senesi (2002) and Kolios and Feidas (2010) used a method based on cloud top brightness temperature. In particular, we found a peak of MCS occurrence in both the North Sea and the Baltic Sea during August and a generally higher MCS occurrence in northern Europe during the warm season compared to Morel and Senesi (2002). Similarly, while the peak of MCS frequency in fall over the eastern Adriatic is expected (Feng et al., 2021; Taszarek et al., 2019), the peak over northwestern Spain is more surprising and was not found in previous studies based on cloud top brightness temperature for MCS identification (Feng et al., 2021; García-Herrera et al., 2005). We believe that the MCSs over the North Sea and the Baltic Sea in late summer, and those over northwestern Spain during the cold season, are due to less deep convective systems, that may not satisfy the IR criteria but have a large area and still produce CGs.

Thus, MCSs affect many regions over Europe throughout the year, and, due to their convective nature and their large spatial extent, MCSs often generate large amounts of precipitation both in time and space (e.g., Schumacher

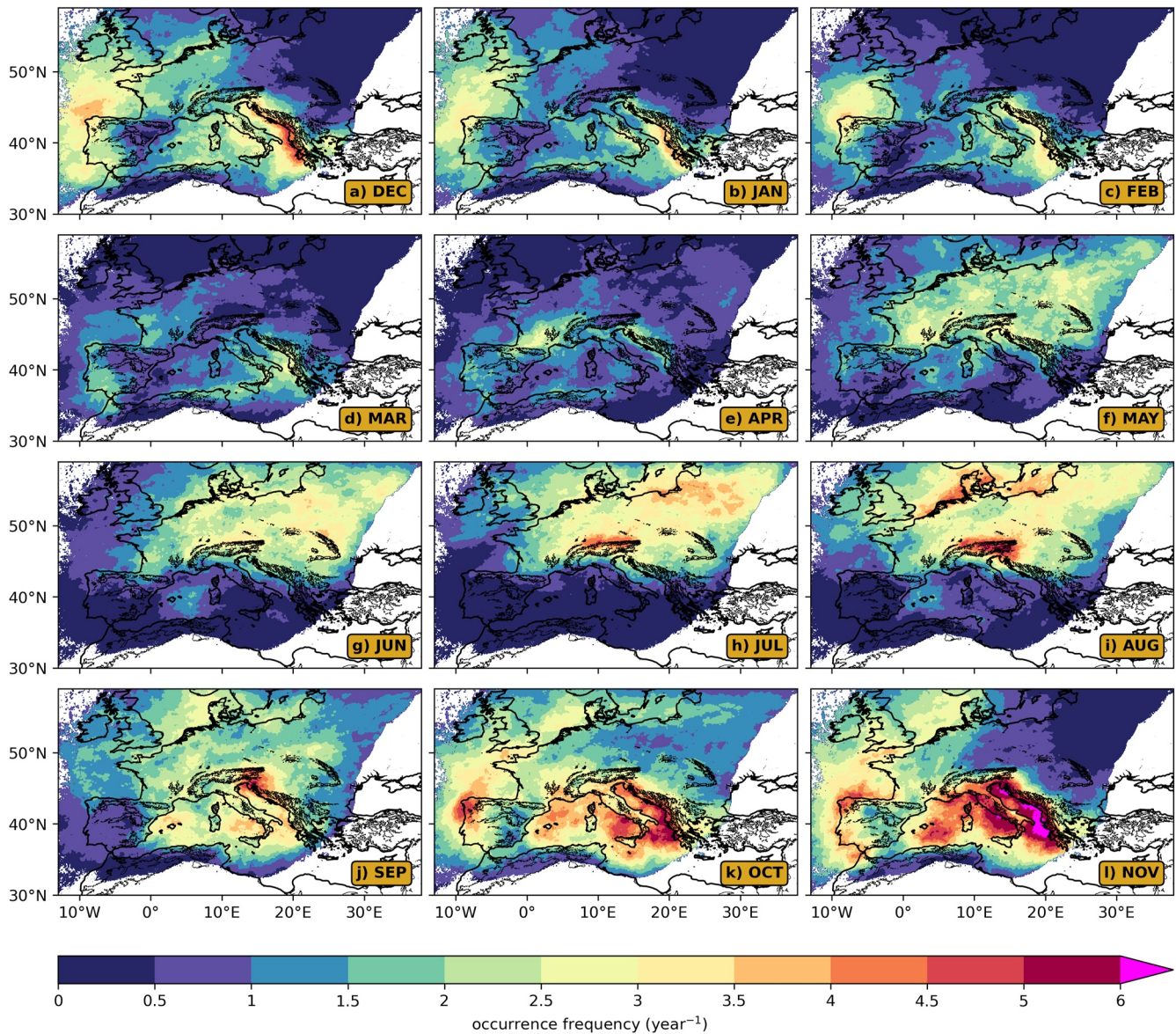


Figure 4. Averaged number of mesoscale convective systems (MCSs) per year by month (a–l). White areas represent missing values, defined as points with means of less than one CG per year.

and Johnson, 2005). In the following, we quantify their contribution to total and extreme precipitation for each season (DJF, MAM, JJA, and SON).

3.3. Substantial MCS Contributions to Precipitation Totals

MCSs account for substantial precipitation amounts exceeding 100 mm in a single season over large areas, which often corresponds to more than a third of the total precipitation in this season (Figure 5). Overall, MCS precipitation dominates convective precipitation (Figure S6 in Supporting Information S1) and its spatial patterns are generally commensurate with those of MCS frequency in the previous section (Figure 4) and those of the mean precipitation climatology (Figure S5 in Supporting Information S1). There are however smaller scale differences that can be attributed to the average spatial distribution of precipitation within individual MCSs.

In winter and to a lesser extent in fall, precipitation totals stemming from MCSs tend to peak offshore along the coasts, a pattern that is even more pronounced for isolated convection (Figure S7 in Supporting Information S1)

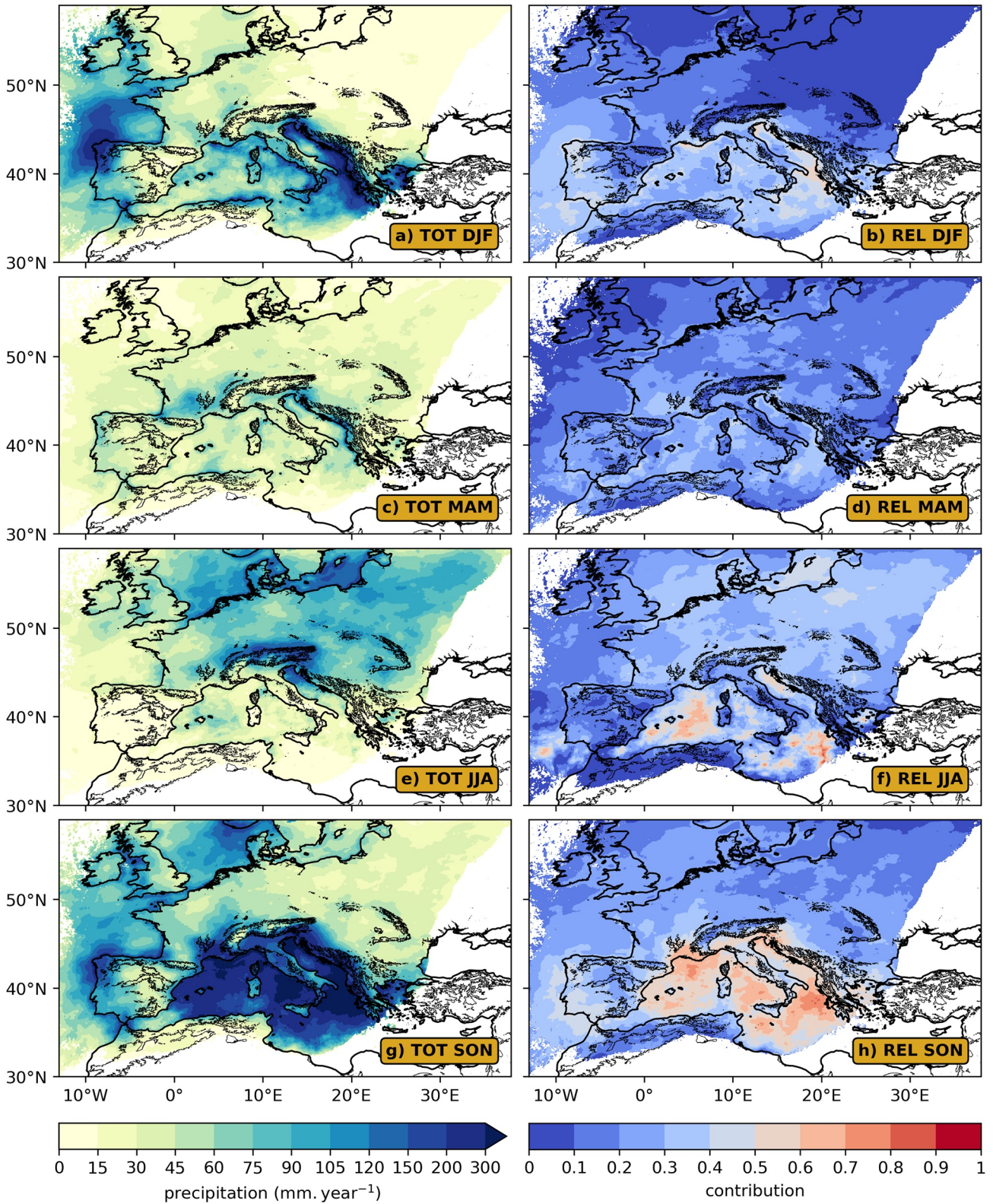


Figure 5. Total MCS precipitation per year (in mm yr⁻¹, left column) and contribution of mesoscale convective systems (MCSs) to total precipitation (right column) over Europe in winter (DJF, a, b), spring (MAM, c, d), summer (JJA, e, f), and fall (SON, g, h).

and suggesting a role of the land-sea contrasts for MCS triggering in these seasons. By compositing over events over several coasts in fall and winter (Text S3, Figures S8, and S9 in Supporting Information S1), we find that the occurrence of precipitation along these coasts is often associated with enhanced low level winds from sea to land, suggesting enhanced moisture convergence by the reduction of wind speed when propagating inland; for example, due to increased surface roughness, the presence of topography, or the encounter of the land breeze front (Malda et al., 2007; Wang & Sobel, 2017). We find this effect to be a characteristic of most coastal MCSs and isolated convective events.

The regions most affected by MCS precipitation are eastern Adriatic, western Italy, and south eastern France during fall, with the contribution from MCS precipitation exceeding 300 mm on average, which corresponds to 50–80% of the total precipitation. Northwestern Spain also exhibits a pronounced peak exceeding 200 mm in both fall and winter, yielding a contribution of 40–50% to total precipitation. This region, and more generally most of northern Europe is also significantly impacted by stratiform precipitation which likely stems from Atlantic low-pressure systems (Figure S10 in Supporting Information S1), explaining relatively low MCS contributions to total precipitation, there. In spring, MCS precipitation amounts are more homogeneous between continents and seas, reaching about 30–50 mm over large areas, which corresponds to 10–40% of total precipitation. The summer MCS precipitation peaks at about 200 mm over the mountain ranges and the northern Seas of Europe, which corresponds to about a third of the seasonal total precipitation in these areas.

3.4. Extreme Precipitation Dominated by MCSs

One of the most common hazards resulting from MCSs is their tendency to generate intense precipitation accumulations over extended regions. It is however worth noting that extreme precipitation accumulations may also arise from for example, stationary isolated convective systems (Bauer-Messmer et al., 1997). To quantify the MCS contribution to extreme precipitation accumulations we first derive the 98th percentile of event-based precipitation accumulations from individual PFs (both MCS and non-MCS PFs) and from non-PFs for each pixel (displayed in Figure 6). Here, events are defined as a sequence of consecutive IMERG time steps with strictly positive precipitation intensity (see Text S4 in Supporting Information S1 for further details on the methodology). One can see that the PFs tend to produce heavy rain accumulations over the Mediterranean in all seasons but especially during fall and winter where the 98th percentile of precipitation accumulation due to individual PFs exceeds 50 mm along the coasts. Most of the coastal areas exhibit maxima in extreme precipitation accumulations, as noticed for both isolated convective and MCS precipitation totals (Figure 5 and Figure S7 in Supporting Information S1).

For each pixel, we then select all PFs that produce precipitation exceeding the 98th percentile of precipitation accumulation of this single pixel. By determining the fractional contribution from MCSs (Figure 6) we show that MCSs impact more strongly on extreme precipitation events than the mean. In some parts of the Mediterranean and the southern Iberian Peninsula, nearly all extreme precipitation stems from MCS in fall and this contribution remains high (>60%) during winter. Although MCSs are not particularly frequent in spring, they still significantly contribute to extremes in most of continental Europe. In this season, the remainder of extreme precipitation events is due to stratiform (around 40%, Figure S11 in Supporting Information S1) and isolated convective precipitation (around 25%, Figure S12 in Supporting Information S1). In summer, more than half of precipitation accumulation extremes in continental Europe are due to MCSs whereas the remaining 50% are due to isolated convective (Figure S12 in Supporting Information S1) and stratiform events (Figure S11 in Supporting Information S1), with a similar share between these two (around 25%). We also found that the magnitude of the MCS contribution to precipitation extreme accumulation is highly dependent to the percentile used for the definition of extreme precipitation accumulation, with higher percentiles being systematically associated with larger contributions (not shown).

Summing up, MCSs generally dominate precipitation accumulation extremes over most of Europe, with only northern Europe during winter as an exception.

3.5. Diurnal Cycle—Large Contrasts Between Coasts and Continents

Often poorly represented by numerical models (Brockhaus et al., 2008), the diurnal cycle of precipitation is of key mechanistic and practical relevance. For each of the subregions (Figure 1) and each month, we compute

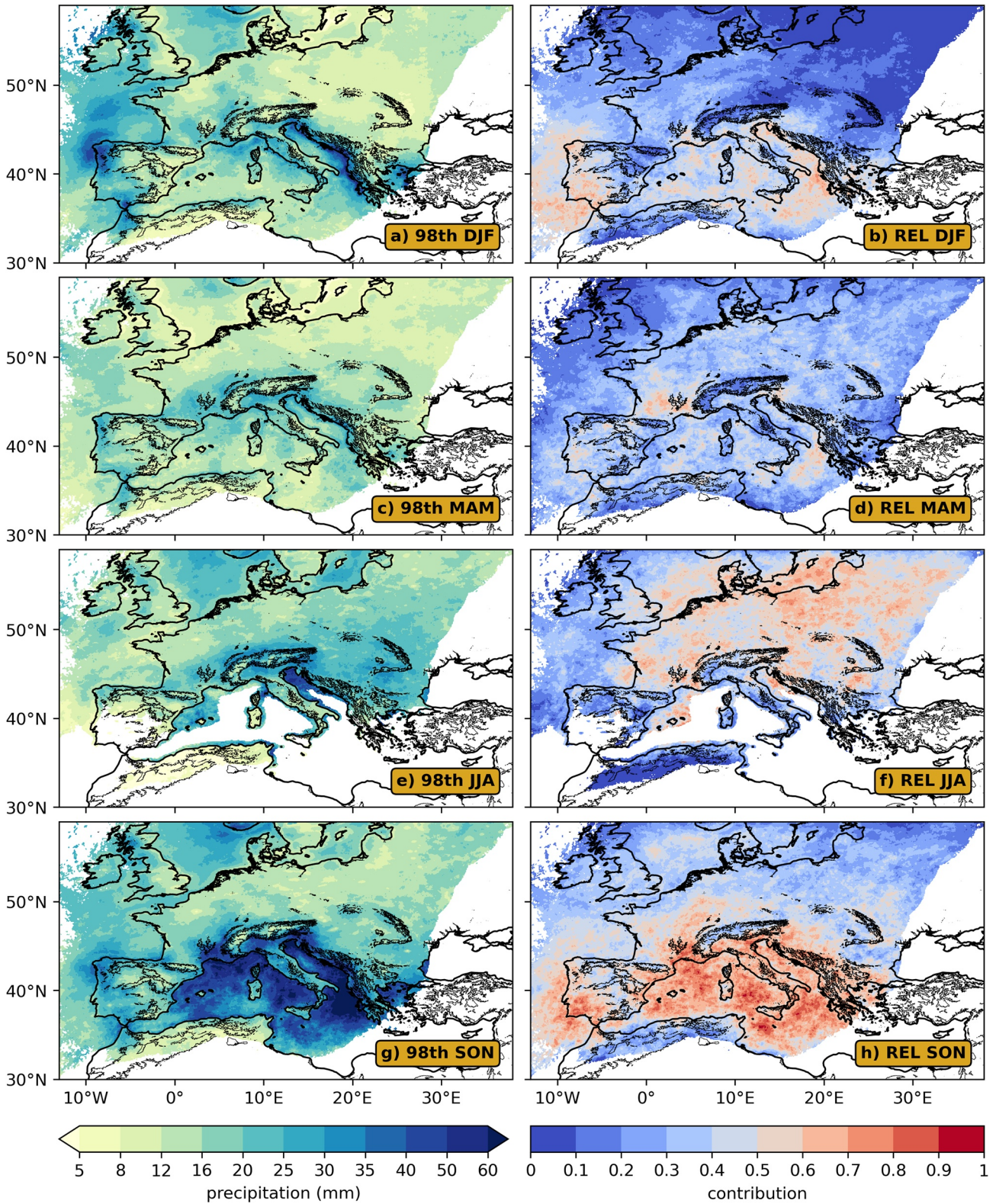


Figure 6. 98th percentile of event-based precipitation accumulations (in mm, left column) and contribution of mesoscale convective systems (MCSs) to the precipitation events producing the 2% most extreme precipitation accumulations (as defined in Section 3.4, right column) over Europe in winter (DJF, a, b), spring (MAM, c, d), summer (JJA, e, f) and fall (SON, g, h). White areas are missing data, that is, points with an insufficient number of events (Section 3.4) or with means of less than one CG per year.

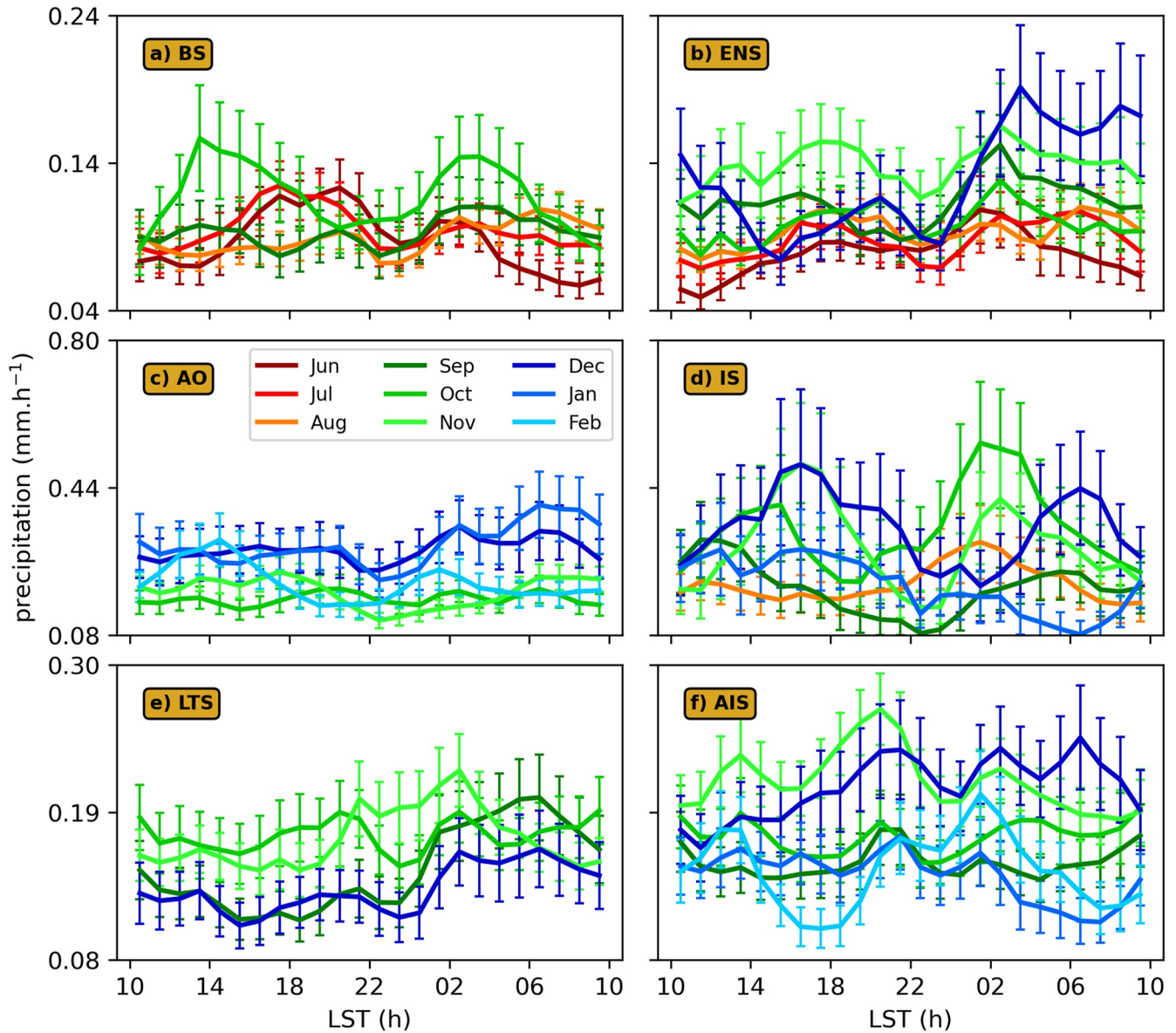


Figure 7. Monthly expected values of mesoscale convective system (MCS) precipitation (in mm hr^{-1}) conditioned on MCS occurrence within the coastal subregions as a function of local solar time (LST) (in hr): Baltic Sea (BS) (a), English channel and North Sea (ENS) (b), Atlantic Ocean (AO) (c), Irish Sea (IS) (d), Ligurian and Tyrrhenian Seas (LTS) (e), and Adriatic and Ionian Seas (AIS) (f) (see Figure 1). Results are given for months with the main MCS activity according to Figure 4. For each LST bin the standard error is calculated to estimate the uncertainty in the mean and represented by error bars.

the climatological diurnal cycle of the expected value of MCS precipitation given the occurrence of an MCS in the subregion at any time of the day. In detail, we collect the MCS precipitation intersecting the subregion, average over the subregion, and stratify and accumulate by local solar time (LST) 1-hr bins. For each bin, we sum the MCS hourly precipitation and divide by the number of MCS affecting the subregion at any time of the day. Finally, we select the months of peak MCS activity according to the monthly number distribution shown in Figure 4.

3.5.1. Large Intermonth and Interregional Variability in Coastal Regions

For the coastal subregions (BS, ENS, AO, IS, LTS, and AIS) the diurnal cycle of MCS precipitation varies strongly between subregions and seasons (Figure 7). Some subregions (BS in June, July, October; ENS in November; AO in February; IS in October, November, and December) exhibit afternoon peaks of MCS precipitation, which we ascribe to convection triggered over the continent. We however note that the amplitude of these peaks

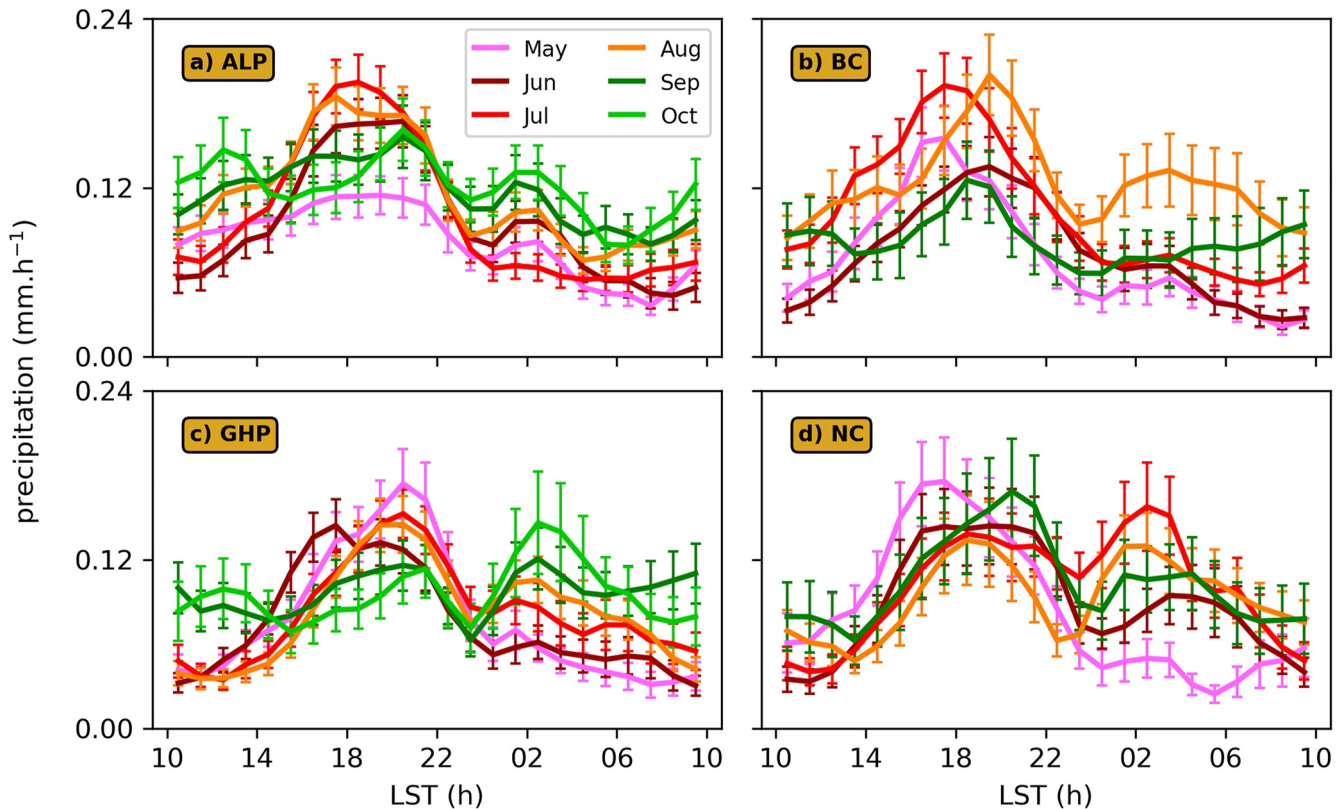


Figure 8. Similar as Figure 7 but for the continental subregions: Alps (ALP) (a), Baltic Sea (BS) (b), Great Hungarian Plain (GHP) (c), and north Carpathian (NC) (d) (see Figure 1).

is not commensurate with the amplitude of the solar diurnal cycle, for example, IS experiences the strongest afternoon peak of MCS precipitation during the month with the least diurnal variation in solar irradiance of the year (December). While identifying the nature of this discrepancy is beyond the scope of this study, this observation reveals the presence of other seasonally varying mechanisms that may enhance or inhibit the “natural” (thermally driven) diurnal cycle of organized convection in coastal regions. A number of subregions (BS in October; ENS from September to December; AO in December and January; IS in October and November; LTS in September, October, and December; AIS in February) exhibit a nocturnal/early morning peak, reminiscent of the total precipitation diurnal cycle over most sea areas (Bowman et al., 2005; Dai, 2001; Tan et al., 2019; Watters & Battaglia, 2019). We note that this nocturnal/early morning precipitation peak is not present in every coastal subregion, for every month of the year and for every type of precipitation (Figures S13–S15 in Supporting Information S1), which also suggests that different mechanisms may be involved.

3.5.2. Nocturnal Peaks in Continental Regions

The diurnal cycle analysis was repeated for the continental subregions for May to October (Figure 8). There, a generally more pronounced MCS diurnal cycle is found, exhibiting reduced intermonth variability compared to the coastal areas. In the four continental subregions there is a strong late afternoon peak of MCS precipitation from May to August. This peak is most pronounced during July over ALP and BC, whereas it is more marked in May in GHP and NC. We note that this peak tends to occur later (around 20 LST) in the lee of the Alps (in GHP) and the lee of the Carpathians (in NC), compared to the Alps and the Baltic plains (BC; around 18 LST). This characteristic might be explained by propagating systems from the mountains toward the plains, where convective activity may therefore occur later in the evening (as for the MCS presented in Figure 2d). Bao and Zhang (2013) observed such convective systems forming in the afternoon at the eastern edge of the northern China mountain ranges, due to the thermally driven mountain-plains solenoid (MPS) circulation, propagating downslope, and peaking in the evening through cold pool dynamics. Further studies are required to determine if similar processes occur in the vicinity of the Alps and Carpathians during summer and explain the delayed MCS precipitation peak

over the lee regions. We also find that isolated convective precipitation tends to peak earlier in the afternoon than MCS (Figure S16 in Supporting Information S1), consistent with the time required for the upscale growth of MCSs. Generally weaker diurnal ranges of MCS precipitation are observed during September and October (as observed for total precipitation in Mandapaka et al. (2013) and Alber et al. (2015)).

Interestingly, for the GHP subregion, the diurnal cycle of MCS precipitation exhibits another systematic peak (at around 3 LST). This nocturnal peak becomes more and more pronounced when moving from May to October, as opposed to the late afternoon peak, which diminishes in the course of this seasonal period. A secondary nocturnal peak also appears for the other continental subregions, even though it is less pronounced and systematic. As seen previously (Figure 4), the Adriatic Sea is a region of intense MCS activity in late summer and fall. Therefore, one could argue that the nocturnal MCS precipitation peak in GHP might be related to the Adriatic Sea diurnal cycle, “leaking” into GHP at nighttime as a result of a southwesterly flow. However, as seen in Figure 7g and Figure S13g in Supporting Information S1, there is no evidence for a clear evening or nocturnal peak in both MCS and isolated convective precipitation for AIS during these months. We further note that the nocturnal peak is generally less pronounced or does not appear in isolated convective precipitation (Figure S16 in Supporting Information S1), as well as for stratiform precipitation and CGs (Figures S17 and S18 in Supporting Information S1). Levizzani et al. (2010) evidenced a slight nocturnal peak of cold cloud frequency in August over similar longitudes, mentioning a potential role of the Carpathians in enhancing precipitating systems. Twardosz (2007) analyzed the diurnal cycle of precipitation over southern Poland conditional on different circulation types and noted a nocturnal/early morning peak of precipitation associated with warm fronts in southerly to southwesterly flows. It is however uncertain whether nocturnal MCSs in this region are regularly embedded within a warm front, when warm fronts are usually associated to less convectively unstable environments (as noted in Twardosz (2010)). The precise origin of MCS nocturnal precipitation peaks over the European continental areas thus remains uncertain and requires further studies.

4. Understanding the Spatiotemporal Distribution of European MCSs

It was found that MCSs often develop near frontal boundaries which provide dynamical lifting over large scales (e.g., Maddox (1983)). Here, we estimate the frontal activity by using the method of Parfitt et al. (2017) on ERA5 data to identify “frontal grid points” in the middle troposphere (600 hPa; to avoid the detection of low level breeze fronts). We define fronts as contiguous frontal pixels with a horizontal extent of at least 300 km. To only select synoptic fronts from low-pressure systems, we discard fronts containing less than 4 ERA5 pixels with a negative anomaly (from 2000 to 2020 climatology) of sea level pressure and geopotential height at 500 hPa. By calculating the proportion of frontal pixels (relative to the total number of pixels) as a function of the distance from a PF at the time of its largest extent (Figure S19 in Supporting Information S1), we find that MCSs are more tightly connected to the presence of a frontal boundary at few hundreds of km from their center than for isolated convective and stratiform PFs. Among these fronts, the contribution of cold fronts dominates by a factor of two compared to warm fronts (not shown). We note that cold fronts may trigger MCSs directly along their boundary or less directly through for example, the formation of prefrontal disturbances (Schultz, 2005).

In the remainder of this section, we analyze the MCS precipitation annual cycle for the different subregions (Figure 1) in relation to the SST (or land 2-m temperatures for continental subregions), the frequency of significant CAPE, and frontal occurrence. CAPE is considered significant when it exceeds a threshold of 100 J kg^{-1} (consistent with Figure S3 in Supporting Information S1). We evaluate frontal occurrence as follows: for each pixel within each subregion we count the number of times a front occurred over each month. If a pixel is part of two fronts that are separated by less than 3 hr, it is assumed that it is the same front. This front occurrence frequency is then averaged over the box and the 16 years.

4.1. Coastal Drivers: Dynamics

In all coastal locations, SSTs generally peak in August, as does CAPE. The similarity in annual cycles of SSTs and CAPE is consistent with previous studies reporting a strong influence of SSTs on CAPE (Cheng et al., 2022; Fu et al., 1994; Johnson & Xie, 2010). For the northern coasts of Europe, BS and ENS, these peaks coincide with those of MCS precipitation, suggesting that moisture availability and convective instability might play a determining role in MCS precipitation there. This applies particularly to BS, where the rapid SST decrease after August is accompanied by a rapid decay of CAPE. For ENS the drop in SSTs is more gradual, limiting the decay of CAPE in fall. This, associated with increased frontal activity, may extend the appearance of the MCS precipitation peak until November in ENS. For all remaining coastal regions, the MCS precipitation peak is delayed

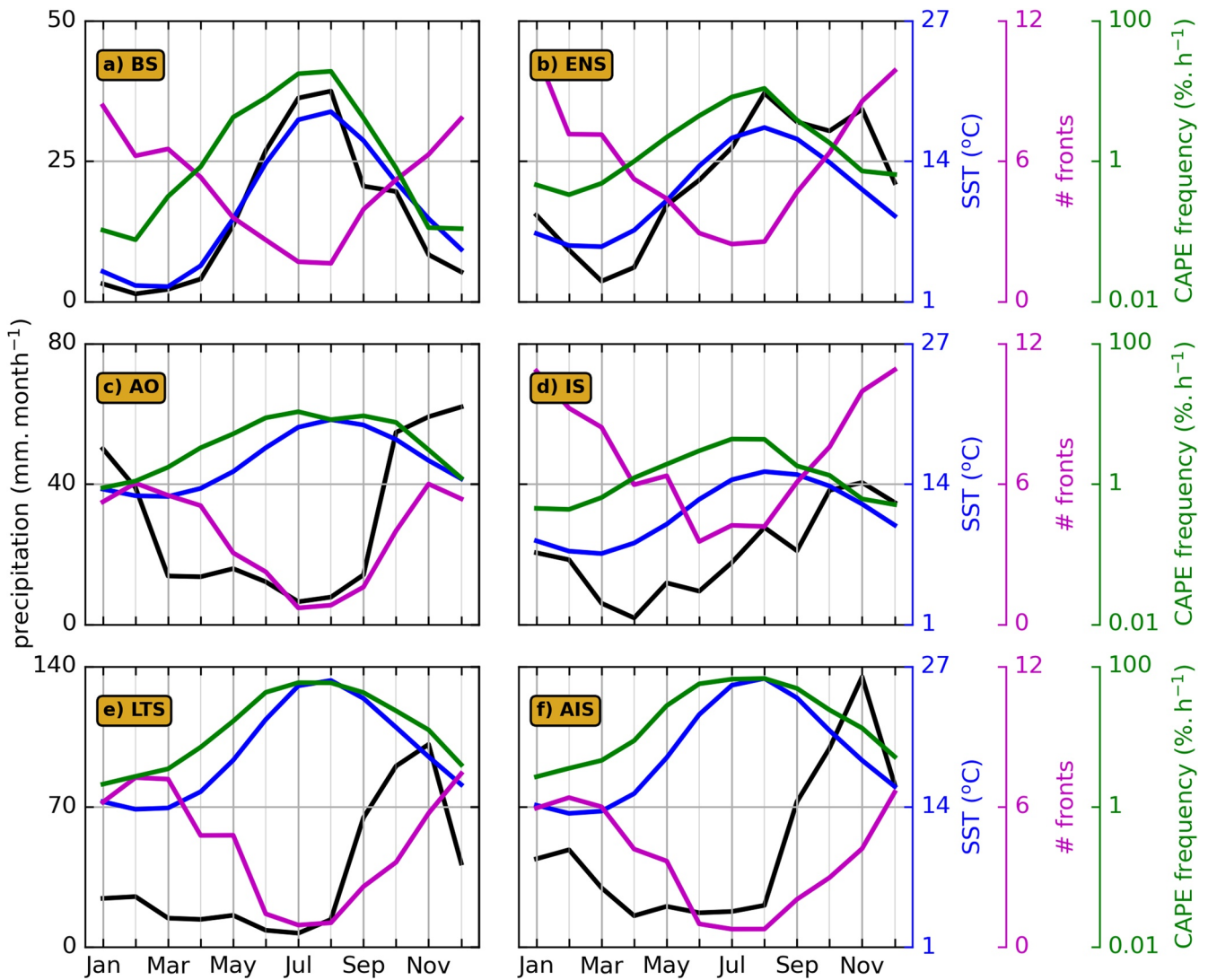


Figure 9. Averaged monthly time series of Multisatellite Retrievals for Global Precipitation Measurement (IMERG) mesoscale convective system (MCS) precipitation amounts (in mm month^{-1} , black), ERA5 Sea Surface Temperature (SST, in degrees Celsius, blue), number of fronts (magenta) and Convective Available Potential Energy (CAPE) frequency (defined in Section 4; in $\% \text{ hr}^{-1}$, green; note the logarithmic scale) for the coastal subregions: Baltic Sea (BS) (a), English channel and North Sea (ENS) (b), Atlantic Ocean (AO) (c), Irish Sea (IS) (d), Ligurian and Tyrrhenian Seas (LTS) (e), and Adriatic and Ionian Seas (AIS) (f) (see Figure 1).

relative to the August SST and CAPE peaks: November for the Mediterranean coasts (LTS and AIS), October for IS and December for AO. Unlike BS and ENS, these regions experience higher SSTs in August that decrease progressively during fall, hence convection in these regions might be less constrained by CAPE availability in fall. Rather, the lack of triggering and organizing large-scale patterns, such as fronts, in concert with a high Convective Inhibition (CIN, Figure S20 in Supporting Information S1), may be limiting factors in these regions during late spring and summer. Over BS, ENS, LTS, and AIS, we attribute the decrease in MCS activity in winter or early spring to CAPE limitations. While the exact origin of the drop in MCS precipitation over AO and IS during early spring remains uncertain, decaying land-sea thermal contrasts (Figure S20 in Supporting Information S1) could weaken breeze circulations and potentially MCS triggering in this season (Malda et al., 2007; Wang & Sobel, 2017).

4.2. Continental Drivers: Thermodynamics

In contrast to the coastal regions, inland MCS precipitation peaks generally coincide with peaks in surface temperature, that is, July for BC and NC and August for ALP and GHP, despite a relatively low front frequency

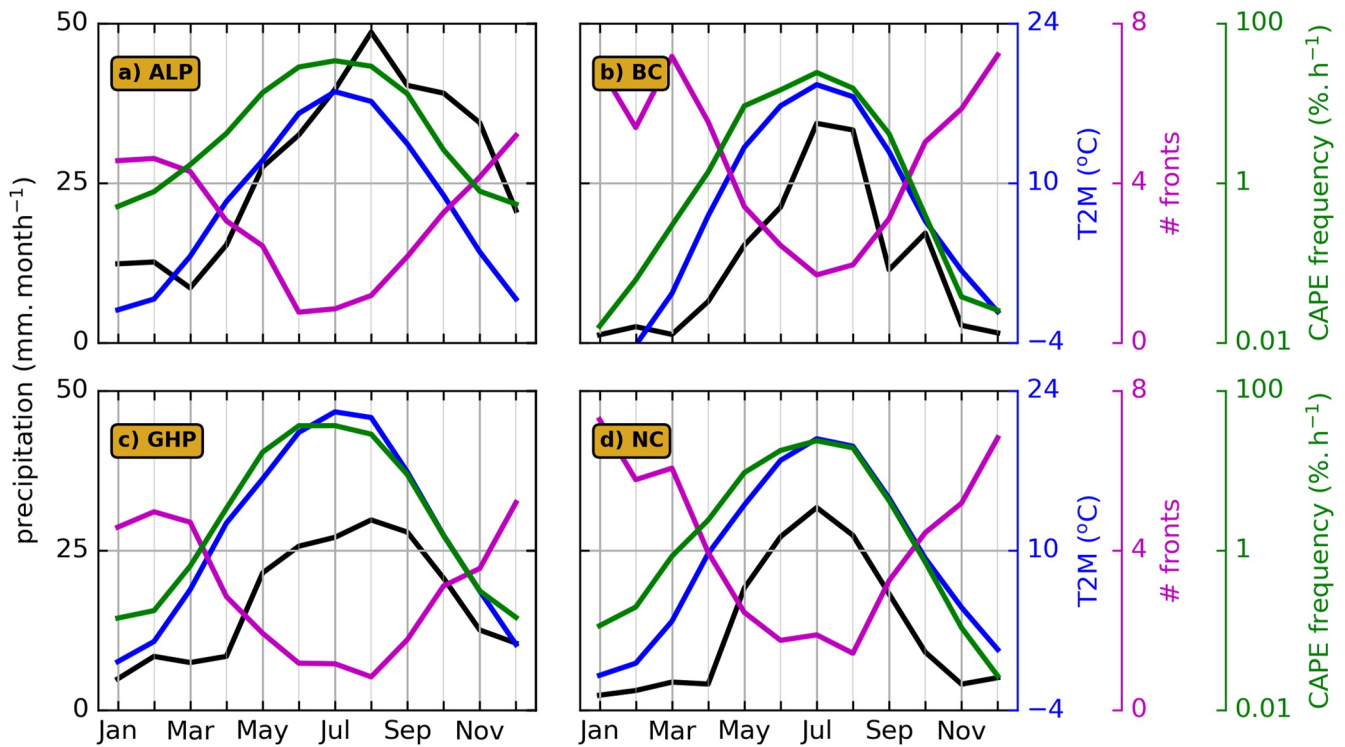


Figure 10. Similar as Figure 9 but for the continental subregions substituting ECMWF Atmospheric Reanalysis Version 5 (ERA5) Sea Surface Temperatures (SSTs) by ERA5 2-m Temperatures: Alps (ALP) (a), Baltic Continent (BC) (b), Great Hungarian Plain (GHP) (c), and north Carpathian (NC) (d) (see Figure 1).

and a substantial CIN (Figure S21 in Supporting Information S1), suggesting a more thermodynamic control (Figure 10). We interpret this as resulting from land surfaces often constituting topographic boundaries that force large-scale convection without the need for an air mass boundary. We note that CAPE frequency maxima generally occur slightly earlier in the year (typically in July). ALP and GHP show a long tail in fall despite deteriorating thermodynamic and instability conditions. This persistent MCS activity during fall might be related to Mediterranean unstable air masses that are advected toward the Alps and Balkans, and eventually leading to MCS formation by topographic lifting or MCS advection (e.g., Davolio et al. (2016)).

5. Summary and Conclusions

We have characterized MCSs over Europe by building a long-term MCS climatology (16 years) at high spatial resolution (0.1°). MCSs are identified by detecting and tracking precipitation features using the recent IMERG satellite-based data set and conditioning on lightning data from the EUCLID data set. MCSs are abundant and responsible for substantial precipitation totals in all seasons. In fall and winter, MCSs are mainly concentrated over the Mediterranean and the Atlantic coasts, whereas in summer, MCSs mainly affect continental Europe, especially mountainous regions, and the northern seas. Spring is transitional, with MCS activity moving inland and pole-ward.

The contribution of MCSs to total precipitation peaks over the Mediterranean during fall, exceeding 70% over large areas. While many other regions are also significantly affected by stratiform precipitation, the MCS contribution often reaches similar amplitudes over the hotspot regions. Concerning extremes, MCSs contribute even more strongly, exceeding 90% in the Mediterranean in fall and 70% over northern Europe in summer.

The diurnal cycle of MCS precipitation over coastal areas exhibits large intermonth and interregional variability, far from a systematic nocturnal/early morning maximum expected from the climatology (Watters & Battaglia, 2019), and suggesting that different mechanisms are involved. The MCS precipitation diurnal cycle over the selected continental subregions shows a more pronounced and systematic diurnal cycle during the warmest months of the year. For these months we find a late afternoon/evening peak for MCSs, following the afternoon peak of isolated convective. In some of the locations (particularly in the Great Hungarian Plain in early

fall), we find an additional nocturnal maximum, despite reduced convective instability. The exact origin of this striking feature remains unclear and begs for further investigation, such as through high-resolution simulation case studies.

We then analyze the MCS annual cycle and associated variables, finding that, across subregions, convective instability peaks in summer whereas frontal activity, for which we found an overall strong involvement in MCS activity, peaks in the winter. Two main features stick out.

- In subregions where convective instability is a limiting factor and decreases rapidly from summer to fall, MCS precipitation peaks concomitantly with the peak of convective instability and surface temperature. This is the case for the continental regions and the Baltic and North Seas.
- In subregions where the convective instability has a more gradual decrease or remains significant in fall, MCS precipitation tends to peak in fall. We further attribute this delay to more favorable dynamical conditions, namely more pronounced frontal activity. This is the case of the large water bodies of high-heat capacity, for which the decrease of SSTs during fall is slower. Whereas MCSs do occasionally occur in these regions, the lack of dynamical forcing appears as a limiting factor during summer compared to fall.

In summary, this study highlights the significant role of MCSs in driving total, and in particular extreme, precipitation in Europe.

The MCS precipitation nocturnal peak found in the Great Hungarian Plain is reminiscent of previous studies focusing on different continental regions (Geerts et al., 2017; Levizzani et al., 2010; Li et al., 2020; Salio et al., 2007; Twardosz, 2010) and where the nocturnal precipitation maximum is attributed to both the nocturnal peak of the LLJ and the reversal of the MPS circulation during the night (e.g., Carbone & Tuttle, 2008; Li et al., 2020; Salio et al., 2007). While these processes may be accounting for the nocturnal MCS precipitation peak over the Great Hungarian Plain, they are insufficient in explaining its stronger amplitude during fall. Analyzing several heavy precipitation events over northeastern Italy during fall, Davolio et al. (2016) found that the propagation of intense convective systems from the coasts to the mountains is characterized by the progressive removal of a northeasterly barrier wind blocking the warm low level southeasterly flow from the Adriatic Sea. As northeastern Italy is a region of intense MCS activity during fall (as noted) and is located directly upstream of the Great Hungarian Plain, studying the diurnal cycle of such transition of regimes may provide further insights on the nocturnal maximum of MCS precipitation over the Great Hungarian Plain in fall.

As noted, identification and tracking errors may exist in our tracking algorithm, notably from missed precipitation features overlaps between consecutive time steps or from inherent IMERG deficiencies regarding the MCS precipitation estimates (e.g., Cui et al., 2020). In these aspects, further improvements of the algorithm could be made for example, by predicting the motion of individual precipitation features (e.g., as Heikenfeld et al., 2019) and checking for potential overlaps with the predicted position. A new version of the algorithm could also correct the IMERG estimates to reduce the precipitation false alarms in the vicinity of MCS anvils (as proposed in Cui et al. (2020)).

Unlike previous studies, our MCS detection algorithm has the specificity of using cloud to ground lightning flashes to discriminate between convective and nonconvective precipitation features. It enables our algorithm to include large frontal thundery rainbands and warm cloud/low-topped convective clusters in the definition of MCSs, which may be missed by methods combining cloud top brightness temperatures with thresholds on the precipitation field. Whether these “ambiguous” systems should be classified as MCS is debatable (Feng et al., 2021) and beyond the scope of this study. However, comparing our results with Feng et al. (2021), in which these systems are purposely excluded from the MCS definition, we find substantially higher MCS contributions to total and extreme precipitation over Europe, especially in the northern seas and the near Atlantic, suggesting important contributions from these systems. Some of these systems may be embedded into atmospheric rivers (as suggested by Feng et al. (2021)), which are well known for being associated with heavy precipitation and floods (Rutz et al., 2019). Therefore, a better understanding of these systems is crucial, especially as the overall intensity of MCSs is projected to increase in a future warmer climate (Chan et al., 2023).

We advocate studies unveiling the mechanisms leading to extreme MCS precipitation and their local characteristics, such as the nocturnal MCS precipitation enhancement over eastern Europe, diurnal cycle variability in coastal regions, and the role of the topography, microphysics, and radiation. Such studies could combine higher resolution precipitation data sets, for example, radar, with numerical simulations to explore local effects. Such

endeavors may ultimately lead to a better causal understanding and thus improved forecasting of midlatitude MCS precipitation extremes.

Data Availability Statement

ERA5 reanalysis data were downloaded from <https://doi.org/10.24381/cds.bd0915c6> and <https://doi.org/10.24381/cds.adbb2d47>. The IMERG precipitation product was downloaded from <https://doi.org/10.5067/GPM/IMERG/3B-HH/06> (Huffman et al., 2019). The surface synoptic observation (SYNOP; O'Brien (2008)) was downloaded from <https://catalogue.ceda.ac.uk/uuid/9f80d42106ba708f92ada730ba321831>. The EUCLID data are available upon request from <https://www.euclid.org/#>. Topography data were supplied by the GEBCO Compilation Group (2022) GEBCO_2022 Grid (<https://doi.org/10.5285/e0f0bb80-ab44-2739-e053-6c86abc0289c>).

Acknowledgments

The authors gratefully acknowledge funding by the European Research Council (ERC) under the European Union's Horizon 2020 research and innovation program (Grant 771859). JOH further acknowledges funding by a grant from the VILLUM Foundation (Grant 13168) and the Novo Nordisk Foundation Interdisciplinary Synergy Program (Grant NNF19OC0057374). This work used resources of the Deutsches Klimarechenzentrum (DKRZ), granted by its Scientific Steering Committee (WLA) under project ID bb1166. The authors would like to thank three anonymous reviewers for their insightful comments on earlier drafts of this manuscript. Open Access funding enabled and organized by Projekt DEAL.

References

- Adler, R. F., Sapiano, M. R., Huffman, G. J., Wang, J.-J., Gu, G., Bolvin, D., et al. (2018). The global precipitation climatology project (GPCP) monthly analysis (new version 2.3) and a review of 2017 global precipitation. *Atmosphere*, 9(4), 138. <https://doi.org/10.3390/atmos9040138>
- Alber, R., Jaagus, J., & Oja, P. (2015). Diurnal cycle of precipitation in Estonia. *Estonian Journal of Earth Sciences*, 64(4), 305. <https://doi.org/10.3176/earth.2015.36>
- Ashley, W. S., Haberlie, A. M., & Strohm, J. (2019). A climatology of quasi-linear convective systems and their hazards in the United States. *Weather and Forecasting*, 34(6), 1605–1631. <https://doi.org/10.1175/WAF-D-19-0014.1>
- Bao, X., & Zhang, F. (2013). Impacts of the mountain-plains solenoid and cold pool dynamics on the diurnal variation of warm-season precipitation over northern China. *Atmospheric Chemistry and Physics*, 13(14), 6965–6982. <https://doi.org/10.5194/acp-13-6965-2013>
- Bauer-Messmer, B., Smith, J. A., Baeck, M. L., & Zhao, W. (1997). Heavy rainfall: Contrasting two concurrent great plains thunderstorms. *Weather and Forecasting*, 12(4), 785–798. [https://doi.org/10.1175/1520-0434\(1997\)012<0785:HRCTCG>2.0.CO;2](https://doi.org/10.1175/1520-0434(1997)012<0785:HRCTCG>2.0.CO;2)
- Berg, P., & Haerter, J. (2013). Unexpected increase in precipitation intensity with temperature—A result of mixing of precipitation types? *Atmospheric Research*, 119, 56–61. <https://doi.org/10.1016/j.atmosres.2011.05.012>
- Bowman, K. P., Collier, J. C., North, G. R., Wu, Q., Ha, E., & Hardin, J. (2005). Diurnal cycle of tropical precipitation in tropical rainfall measuring mission (TRMM) satellite and ocean buoy rain gauge data. *Journal of Geophysical Research*, 110, D21104. <https://doi.org/10.1029/2005JD005763>
- Brockhaus, P., Luthi, D., & Schar, C. (2008). Aspects of the diurnal cycle in a regional climate model. *Meteorologische Zeitschrift*, 17(4), 433–444. <https://doi.org/10.1127/0941-2948/2008/0316>
- Carbone, R. E., & Tuttle, J. D. (2008). Rainfall occurrence in the U.S. warm season: The diurnal cycle. *Journal of Climate*, 21(16), 4132–4146. <https://doi.org/10.1175/2008JCLI2275.1>
- Cecil, D. J., Goodman, S. J., Boccippio, D. J., Zipser, E. J., & Nesbitt, S. W. (2005). Three years of TRMM precipitation features. Part I: Radar, radiometric, and lightning characteristics. *Monthly Weather Review*, 133(3), 543–566. <https://doi.org/10.1175/MWR-2876.1>
- Chan, S. C., Kendon, E. J., Fowler, H. J., Kahraman, A., Crook, J., Ban, N., & Prein, A. F. (2023). Large-scale dynamics moderate impact-relevant changes to organised convective storms. *Communications Earth & Environment*, 4(1), 8. <https://doi.org/10.1038/s43247-022-00669-2>
- Cheeks, S. M., Fueglistaler, S., & Garner, S. T. (2020). A satellite-based climatology of central and southeastern U.S. mesoscale convective systems. *Monthly Weather Review*, 148(6), 2607–2621. <https://doi.org/10.1175/MWR-D-20-0027.1>
- Cheng, K.-Y., Harris, L., Bretherton, C., Merlis, T. M., Bolot, M., Zhou, L., et al. (2022). Impact of warmer sea surface temperature on the global pattern of intense convection: Insights from a global storm resolving model. *Geophysical Research Letters*, 49, e2022GL099796. <https://doi.org/10.1029/2022GL099796>
- Cui, W., Dong, X., Xi, B., Feng, Z., & Fan, J. (2020). Can the GPM IMERG final product accurately represent MCSs' precipitation characteristics over the central and eastern United States? *Journal of Hydrometeorology*, 21(1), 39–57. <https://doi.org/10.1175/JHM-D-19-0123.1>
- Dai, A. (2001). Global precipitation and thunderstorm frequencies. Part II: Diurnal variations. *Journal of Climate*, 14(6), 1112–1128. [https://doi.org/10.1175/1520-0442\(2001\)014<1112:GPATFP>2.0.CO;2](https://doi.org/10.1175/1520-0442(2001)014<1112:GPATFP>2.0.CO;2)
- Da Silva, N. A., Muller, C., Shamekh, S., & Fildier, B. (2021). Significant amplification of instantaneous extreme precipitation with convective self-aggregation. *Journal of Advances in Modeling Earth Systems*, 13, e2021MS002607. <https://doi.org/10.1029/2021MS002607>
- Davolio, S., Volonté, A., Manzato, A., Pucillo, A., Cicogna, A., & Ferrario, M. E. (2016). Mechanisms producing different precipitation patterns over north-eastern Italy: Insights from HyMex-SOP1 and previous events. *Quarterly Journal of the Royal Meteorological Society*, 142(S1), 188–205. <https://doi.org/10.1002/qj.2731>
- Feng, Z., Leung, L. R., Liu, N., Wang, J., Houze, R. A., Jr., Li, J., et al. (2021). A global high-resolution mesoscale convective system database using satellite-derived cloud tops, surface precipitation, and tracking. *Journal of Geophysical Research*, 126, e2020JD034202. <https://doi.org/10.1029/2020JD034202>
- Fowler, H. J., Lenderink, G., Prein, A. F., Westra, S., Allan, R. P., Ban, N., et al. (2021). Anthropogenic intensification of short-duration rainfall extremes. *Nature Reviews Earth & Environment*, 2(2), 107–122. <https://doi.org/10.1038/s43017-020-00128-6>
- Fu, R., Genio, A. D. D., & Rossow, W. B. (1994). Influence of ocean surface conditions on atmospheric vertical thermodynamic structure and deep convection. *Journal of Climate*, 7(7), 1092–1108. [https://doi.org/10.1175/1520-0442\(1994\)007<1092:IOOSCO>2.0.CO;2](https://doi.org/10.1175/1520-0442(1994)007<1092:IOOSCO>2.0.CO;2)
- García-Herrera, R., Hernández, E., Paredes, D., Barriopedro, D., Correoso, J. F., & Prieto, L. (2005). A MASCOTTE-based characterization of MCSs over Spain, 2000–2002. *Atmospheric Research*, 73(3–4), 261–282. <https://doi.org/10.1016/j.atmosres.2004.11.003>
- Geerts, B., Parsons, D., Ziegler, C. L., Weckwerth, T. M., Biggerstaff, M. I., Clark, R. D., et al. (2017). The 2015 plains elevated convection at night field project. *Bulletin of the American Meteorological Society*, 98(4), 767–786. <https://doi.org/10.1175/BAMS-D-15-00257.1>
- Haberlie, A. M., & Ashley, W. S. (2019). A radar-based climatology of mesoscale convective systems in the United States. *Journal of Climate*, 32(5), 1591–1606. <https://doi.org/10.1175/JCLI-D-18-0559.1>
- Haerter, J. O., & Schlemmer, L. (2018). Intensified cold pool dynamics under stronger surface heating. *Geophysical Research Letters*, 45, 6299–6310. <https://doi.org/10.1029/2017GL076874>
- Hayden, L., Liu, C., & Liu, N. (2021). Properties of mesoscale convective systems throughout their lifetimes using IMERG, GPM, WLLN, and a simplified tracking algorithm. *Journal of Geophysical Research: Atmospheres*, 126, e2021JD035264. <https://doi.org/10.1029/2021JD035264>

- Heikenfeld, M., Marinescu, P. J., Christensen, M., Watson-Parris, D., Senf, F., van den Heever, S. C., & Stier, P. (2019). Tobac 1.2: Towards a flexible framework for tracking and analysis of clouds in diverse datasets. *Geoscientific Model Development*, 12(11), 4551–4570. <https://doi.org/10.5194/gmd-12-4551-2019>
- Hersbach, H., Bell, B., Berrisford, P., Hirahara, S., Horányi, A., Muñoz-Sabater, J., et al. (2020). The ERA5 global reanalysis. *Quarterly Journal of the Royal Meteorological Society*, 146(730), 1999–2049. <https://doi.org/10.1002/qj.3803>
- Houze, J., & Robert, A. (2012). Orographic effects on precipitating clouds. *Reviews of Geophysics*, 50, RG1001. <https://doi.org/10.1029/2011RG000365>
- Houze, R. A. (2018). 100 years of research on mesoscale convective systems. *Meteorological Monographs*, 59(17), 17.1–17.54. <https://doi.org/10.1175/AMSMONOGRAPHS-D-18-0001.1>
- Huffman, G. J., Stocker, E. F., Bolvin, D. T., Nelkin, E. J., & Tan, J. (2019). GPM IMERG final precipitation 13 half hourly 0.1 degree × 0.1 degree v06 [Dataset]. Goddard Earth Sciences Data and Information Services Center (GES DISC). <https://doi.org/10.5067/GPM/IMERG/3B-HH/06>
- Jirak, I. L., & Cotton, W. R. (2007). Observational analysis of the predictability of mesoscale convective systems. *Weather and Forecasting*, 22(4), 813–838. <https://doi.org/10.1175/WAF1012.1>
- Jirak, I. L., Cotton, W. R., & McAnelly, R. L. (2003). Satellite and radar survey of mesoscale convective system development. *Monthly Weather Review*, 131(10), 2428–2449. [https://doi.org/10.1175/1520-0493\(2003\)131<2428:SARSOM>2.0.CO;2](https://doi.org/10.1175/1520-0493(2003)131<2428:SARSOM>2.0.CO;2)
- Johnson, N. C., & Xie, S.-P. (2010). Changes in the sea surface temperature threshold for tropical convection. *Nature Geoscience*, 3(12), 842–845. <https://doi.org/10.1038/ngeo1008>
- Kolios, S., & Feidas, H. (2010). A warm season climatology of mesoscale convective systems in the mediterranean basin using satellite data. *Theoretical and Applied Climatology*, 102(1), 29–42. <https://doi.org/10.1007/s00704-009-0241-7>
- Laing, A. G., & Fritsch, M. (1997). The global population of mesoscale convective complexes. *Quarterly Journal of Royal Meteorological Society*, 123(538), 389–405. <https://doi.org/10.1002/qj.49712353807>
- Levizzani, V., Pinelli, F., Pasqui, M., Melani, S., Laing, A. G., & Carbone, R. E. (2010). A 10-year climatology of warm-season cloud patterns over Europe and the mediterranean from Meteosat IR observations. *Atmospheric Research*, 97(4), 555–576. <https://doi.org/10.1016/j.atmosres.2010.05.014>
- Li, P., Moseley, C., Prein, A. F., Chen, H., Li, J., Furtado, K., & Zhou, T. (2020). Mesoscale convective system precipitation characteristics over east asia. part i: Regional differences and seasonal variations. *Journal of Climate*, 33(21), 9271–9286. <https://doi.org/10.1175/JCLI-D-20-0072.1>
- Liu, C., & Zipser, E. J. (2015). The global distribution of largest, deepest, and most intense precipitation systems. *Geophysical Research Letters*, 42, 3591–3595. <https://doi.org/10.1002/2015GL063776>
- Luo, L., Xue, M., & Zhu, K. (2020). The initiation and organization of a severe hail-producing mesoscale convective system in east China: A numerical study. *Journal of Geophysical Research*, 125, e2020JD032606. <https://doi.org/10.1029/2020JD032606>
- MacGorman, D. R., Apostolopoulos, I. R., Lund, N. R., Demetriades, N. W. S., Murphy, M. J., & Krehbiel, P. R. (2011). The timing of cloud-to-ground lightning relative to total lightning activity. *Monthly Weather Review*, 139(12), 3871–3886. <https://doi.org/10.1175/MWR-D-11-00047.1>
- Maddox, R. A. (1983). Large-scale meteorological conditions associated with midlatitude, mesoscale convective complexes. *Monthly Weather Review*, 111(7), 1475–1493. [https://doi.org/10.1175/1520-0493\(1983\)111<1475:L.SMCAW>2.0.CO;2](https://doi.org/10.1175/1520-0493(1983)111<1475:L.SMCAW>2.0.CO;2)
- Malda, D., Vilà-Guerau de Arellano, J., van den Berg, W. D., & Zuurendonk, I. W. (2007). The role of atmospheric boundary layer-surface interactions on the development of coastal fronts. *Annales Geophysicae*, 25(2), 341–360. <https://doi.org/10.5194/angeo-25-341-2007>
- Mandapaka, P. V., Germann, U., & Panziera, L. (2013). Diurnal cycle of precipitation over complex alpine orography: Inferences from high-resolution radar observations. *Quarterly Journal of the Royal Meteorological Society*, 139(673), 1025–1046. <https://doi.org/10.1002/qj.2013>
- Mathias, L., Ermert, V., Kelemen, F. D., Ludwig, P., & Pinto, J. G. (2017). Synoptic analysis and hindcast of an intense bow echo in western Europe: The 9 June 2014 storm. *Weather and Forecasting*, 32(3), 1121–1141. <https://doi.org/10.1175/WAF-D-16-0192.1>
- Morel, C., & Senesi, S. (2002). A climatology of mesoscale convective systems over Europe using satellite infrared imagery. II: Characteristics of European mesoscale convective systems. *Quarterly Journal of Royal Meteorological Society*, 128(584), 1973–1995. <https://doi.org/10.1256/003590002320603494>
- Moseley, C., Berg, P., & Haerter, J. O. (2013). Probing the precipitation life cycle by iterative rain cell tracking. *Journal of Geophysical Research: Atmospheres*, 118, 13361–13370. <https://doi.org/10.1002/2013JD020868>
- Moseley, C., Henneberg, O., & Haerter, J. O. (2019). A statistical model for isolated convective precipitation events. *Journal of Advances in Modeling Earth Systems*, 11, 360–375. <https://doi.org/10.1029/2018MS001383>
- Nesbitt, S. W., Cifelli, R., & Rutledge, S. A. (2006). Storm morphology and rainfall characteristics of TRMM precipitation features. *Monthly Weather Review*, 134(10), 2702–2721. <https://doi.org/10.1175/MWR3200.1>
- O'Brien, C. (2008). Met office (2008): Land synop reports from land stations collected by the met office MetDB system [Dataset]. CEDA Archive. Retrieved from <https://catalogue.ceda.ac.uk/uuid/9f80d42106ba708f92ada730ba321831>
- Oliveira, R., Maggioni, V., Vila, D., & Morales, C. (2016). Characteristics and diurnal cycle of GPM rainfall estimates over the central Amazon region. *Remote Sensing*, 8(7), 544. <https://doi.org/10.3390/rs8070544>
- Parfitt, R., Czaja, A., & Seo, H. (2017). A simple diagnostic for the detection of atmospheric fronts. *Geophysical Research Letters*, 44, 4351–4358. <https://doi.org/10.1002/2017GL073662>
- Parker, M. D. (2008). Response of simulated squall lines to low-level cooling. *Journal of the Atmospheric Sciences*, 65(4), 1323–1341. <https://doi.org/10.1175/2007JAS2507.1>
- Pitchford, K. L., & London, J. (1962). The low-level jet as related to nocturnal thunderstorms over midwest United States. *Journal of Applied Meteorology and Climatology*, 1(1), 43–47. [https://doi.org/10.1175/1520-0450\(1962\)001<0043:TLLJAR>2.0.CO;2](https://doi.org/10.1175/1520-0450(1962)001<0043:TLLJAR>2.0.CO;2)
- Poelmann, D. R., Schulz, W., Diendorfer, G., & Bernardi, M. (2016). The European lightning location system EUCLID—Part 2: Observations. *Natural Hazards and Earth System Sciences*, 16(2), 607–616. <https://doi.org/10.5194/nhess-16-607-2016>
- Pradhan, R. K., Markonis, Y., Vargas Godoy, M. R., Villalba-Pradas, A., Andreadis, K. M., Nikolopoulos, E. I., et al. (2022). Review of GPM IMERG performance: A global perspective. *Remote Sensing of Environment*, 268, 112754. <https://doi.org/10.1016/j.rse.2021.112754>
- Punkka, A.-J., & Bister, M. (2015). Mesoscale convective systems and their synoptic-scale environment in Finland. *Weather and Forecasting*, 30(1), 182–196. <https://doi.org/10.1175/WAF-D-13-00146.1>
- Rigo, T., Berenguer, M., & del Carmen Llasat, M. (2019). An improved analysis of mesoscale convective systems in the western mediterranean using weather radar. *Atmospheric Research*, 227, 147–156. <https://doi.org/10.1016/j.atmosres.2019.05.001>
- Rutz, J. J., Shields, C. A., Lora, J. M., Payne, A. E., Guan, B., Ullrich, P., et al. (2019). The atmospheric river tracking method intercomparison project (ARTMIP): Quantifying uncertainties in atmospheric river climatology. *Journal of Geophysical Research: Atmospheres*, 124, 13777–13802. <https://doi.org/10.1029/2019JD030936>

- Salio, P., Nicolini, M., & Zipser, E. J. (2007). Mesoscale convective systems over southeastern south America and their relationship with the south American low-level jet. *Monthly Weather Review*, *135*(4), 1290–1309. <https://doi.org/10.1175/MWR3305.1>
- Schultz, D. M. (2005). A review of cold fronts with prefrontal troughs and wind shifts. *Monthly Weather Review*, *133*(8), 2449–2472. <https://doi.org/10.1175/MWR2987.1>
- Schulz, W., Diendorfer, G., Pedeboy, S., & Poelman, D. R. (2016). The European lightning location system EUCLID—Part 1: Performance analysis and validation. *Natural Hazards and Earth System Sciences*, *16*(2), 595–605. <https://doi.org/10.5194/nhess-16-595-2016>
- Schumacher, R., & Johnson, R. H. (2005). Organization and environmental properties of extreme-rain-producing mesoscale convective systems. *Monthly Weather Review*, *133*(4), 961–976. <https://doi.org/10.1175/MWR2899.1>
- Schumacher, R., & Rasmussen, K. (2020). The formation, character and changing nature of mesoscale convective systems. *Nature Reviews Earth & Environment*, *1*(6), 300–314. <https://doi.org/10.1038/s43017-020-0057-7>
- Sungmin, O., & Kirstetter, P.-E. (2018). Evaluation of diurnal variation of gpm imerg-derived summer precipitation over the contiguous us using MRMS data. *Quarterly Journal of the Royal Meteorological Society*, *144*(S1), 270–281. <https://doi.org/10.1002/qj.3218>
- Surowiecki, A., & Taszarek, M. (2020). A 10-year radar-based climatology of mesoscale convective system archetypes and derechos in Poland. *Monthly Weather Review*, *148*(8), 3471–3488. <https://doi.org/10.1175/MWR-D-19-0412.1>
- Takahashi, H., Lebsack, M., Luo, Z. J., Masunaga, H., & Wang, C. (2021). Detection and tracking of tropical convective storms based on globally gridded precipitation measurements: Algorithm and survey over the tropics. *Journal of Applied Meteorology and Climatology*, *60*(3), 403–421. <https://doi.org/10.1175/JAMC-D-20-0171.1>
- Tan, J., Huffman, G. J., Bolvin, D. T., & Nelkin, E. J. (2019). Diurnal cycle of IMERG v06 precipitation. *Geophysical Research Letters*, *46*, 13584–13592. <https://doi.org/10.1029/2019GL085395>
- Tan, J., Jakob, C., Rossow, W. B., & Tselioudis, G. (2015). Increases in tropical rainfall driven by changes in frequency of organized deep convection. *Nature*, *519*(7544), 451–454. <https://doi.org/10.1038/nature14339>
- Tan, J., Petersen, W. A., & Tokay, A. (2016). A novel approach to identify sources of errors in IMERG for GPM ground validation. *Journal of Hydrometeorology*, *17*(9), 2477–2491. <https://doi.org/10.1175/JHM-D-16-0079.1>
- Taszarek, M., Allen, J., Púčik, T., Groenemeijer, P., Czernecki, B., Kolendowicz, L., et al. (2019). A climatology of thunderstorms across Europe from a synthesis of multiple data sources. *Journal of Climate*, *32*(6), 1813–1837. <https://doi.org/10.1175/JCLI-D-18-0372.1>
- Taszarek, M., Pilgaj, N., Allen, J. T., Gensini, V., Brooks, H. E., & Szuster, P. (2021). Comparison of convective parameters derived from era5 and merra-2 with rawinsonde data over Europe and north America. *Journal of Climate*, *34*(8), 3211–3237. <https://doi.org/10.1175/JCLI-D-20-0484.1>
- Twardosz, R. (2007). Diurnal variation of precipitation frequency in the warm half of the year according to circulation types in Kraków, south Poland. *Theoretical and Applied Climatology*, *89*(3–4), 229–238. <https://doi.org/10.1007/s00704-006-0268-y>
- Twardosz, R. (2010). A synoptic analysis of the diurnal cycle of thunderstorm precipitation in Kraków (southern Poland). *International Journal of Climatology*, *30*(7), 1008–1013. <https://doi.org/10.1002/joc.1960>
- Varga, Á. J., & Breuer, H. (2022). Evaluation of convective parameters derived from pressure level and native era5 data and different resolution WRF climate simulations over central Europe. *Climate Dynamics*, *58*(5–6), 1569–1585. <https://doi.org/10.1007/s00382-021-05979-3>
- Wang, S., & Sobel, A. H. (2017). Factors controlling rain on small tropical islands: Diurnal cycle, large-scale wind speed, and topography. *Journal of the Atmospheric Sciences*, *74*(11), 3515–3532. <https://doi.org/10.1175/JAS-D-16-0344.1>
- Watters, D., & Battaglia, A. (2019). The summertime diurnal cycle of precipitation derived from IMERG. *Remote Sensing*, *11*(15), 1781. <https://doi.org/10.3390/rs11151781>